

# Hu 1-2: a metal-poor bipolar planetary nebula with fast collimated outflows

X. Fang<sup>1\*</sup>, M. A. Guerrero<sup>1</sup>, L. F. Miranda<sup>1</sup>, A. Riera<sup>2</sup>, P. F. Velázquez<sup>3</sup>, and A. C. Raga<sup>3</sup>

<sup>1</sup>*Instituto de Astrofísica de Andalucía (IAA, CSIC), Glorieta de la Astronomía s/n, E-18008 Granada, Spain*

<sup>2</sup>*Departament de Física i Enginyeria Nuclear, EUETIB, Universitat Politècnica de Catalunya, Comte d'Urgell 187, E-08036 Barcelona, Spain*

<sup>3</sup>*Instituto de Ciencias Nucleares, Universidad Nacional Autónoma de México, Apdo. Postal 70-543, CP: 04510, D. F., Mexico*

Accepted . Received

## ABSTRACT

We present narrow-band optical and near-IR imaging and optical long-slit spectroscopic observations of Hu 1-2, a Galactic planetary nebula (PN) with a pair of [N II]-bright, fast-moving ( $>340 \text{ km s}^{-1}$ ) bipolar knots. Intermediate-dispersion spectra are used to derive physical conditions and abundances across the nebula, and high-dispersion spectra to study the spatio-kinematical structure. Generally Hu 1-2 has high He/H ( $\approx 0.14$ ) and N/O ratios ( $\approx 0.9$ ), typical of Type I PNe. On the other hand, its abundances of O, Ne, S, and Ar are low as compared with the average abundances of Galactic bulge and disc PNe. The position-velocity maps can be generally described as an hour-glass shaped nebula with bipolar expansion, although the morphology and kinematics of the innermost regions cannot be satisfactorily explained with a simple, tilted equatorial torus. The spatio-kinematical study confines the inclination angle of its major axis to be within  $10^\circ$  of the plane of sky. As in the irradiated bow-shocks of IC 4634 and NGC 7009, there is a clear stratification in the emission peaks of [O III], H $\alpha$ , and [N II] in the northwest (NW) knot of Hu 1-2. Fast collimated outflows in PNe exhibit higher excitation than other low-ionization structures. This is particularly the case for the bipolar knots of Hu1-2, with He II emission levels above those of collimated outflows in other Galactic PNe. The excitation of the knots in Hu 1-2 is consistent with the combined effects of shocks and UV radiation from the central star. The mechanical energy and luminosity of the knots are similar to those observed in the PNe known to harbor a post-common envelope (post-CE) close binary central star.

**Key words:** ISM: abundances – ISM: jets and outflows – ISM: planetary nebulae: individual: Hu 1-2

## 1 INTRODUCTION

Planetary nebulae (PNe) represent the last stages in the evolution of low- and intermediate-mass stars, before they turn into white dwarfs. A large fraction of PNe presents complex morphologies, including axisymmetric shells, multipolar lobes, and collimated structures, in sharp contrast with the spherical envelopes typically seen around asymptotic giant branch (AGB) stars (e.g., Olofsson et al. 2010). Somehow, the spherical AGB envelope is transformed into the complex PN shell. *Hubble Space Telescope* (HST) observations have led to the suggestion that the shaping of the most structured young PNe (or proto-planetary nebulae, proto-PNe) could be attributed to the action of high-speed collimated outflows or jets that operate during the late-AGB and/or early post-AGB phase, as they interact with the intrinsically spherical AGB circumstellar envelope (Sahai & Trauger 1998). These observations indicate that

collimated outflows probably also play a crucial role in the shaping and dynamical evolution of PNe (e.g., Dennis et al. 2008; Huarte-Espinosa et al. 2012).

Collimated outflows or jet-like structures have been identified in a significant number of PNe. The origin of collimated outflows is still uncertain, although they are most likely related to the evolution of binary systems, the action of magnetic fields, or both (e.g., Soker 2006; De Marco 2009). Particularly, binary interactions that involve accretion (e.g., Soker 1998; Soker & Livio 1994; Reyes-Ruiz & López 1999; Nordhaus & Blackman 2006; Blackman & Lucchini 2014) have been considered to be a plausible engine to produce the ubiquitous collimated outflows in PNe and proto-PNe (e.g., Balick & Frank 2002). Recently, Tocknell, De Marco & Wardle (2014) constrained the physical properties of the common envelope (CE) interaction using the observed masses and kinematics of jets in four post-CE PNe.

Detailed studies of the spectra of jet-like structures in PNe are scarce, but they generally report strong low-excitation emis-

\* E-mail: fangx@iaa.es

sion lines (particularly from [N II]) combined with high-excitation emission lines (e.g., [O III]; Guerrero et al. 2008; Gonçalves et al. 2009). This notable difference with the spectra of the main nebular shells can be attributed to the combined contributions of ionizing photons from the central star and excitation by shocks. Therefore, these structures are candidates of irradiated shocks, i.e., bow-shocks that are illuminated by ionizing (stellar) fluxes from the post-shock direction (e.g., Hartigan, Raymond & Hartmann 1987).

Hu 1-2 (PN G086.5–08.8), first identified by Humason (1921) and classified as elliptical by Manchado et al. (1996), is a PN with fast, highly collimated outflows. Recently, Miranda et al. (2012a) identified two bipolar compact knots along the main axis of Hu 1-2 with bow-shock-like morphologies. An analysis of the radial velocities and proper motions of these knots showed that they move at velocities  $>340 \text{ km s}^{-1}$ . This velocity is much higher than the expansion velocities of the collimated outflows observed in most PNe (Guerrero et al. 2002). For instance, the bright “Saturn Nebula”, NGC 7009, has an elliptical main nebula with a pair of [N II]-bright outer knots along its major axis (e.g., Gonçalves et al. 2003). Despite the morphological similarities with Hu 1-2, the expansion velocity of  $\sim 60 \text{ km s}^{-1}$  reported for the bipolar knots of NGC 7009 (Reay & Atherton 1985) is much lower than that observed in Hu 1-2, although we recall that the expansion velocity of the knots in NGC 7009 is quite uncertain (Gonçalves et al. 2003).

The high-velocity and bow-shock-like morphology led Miranda et al. (2012a) to conclude that these knots probably represent bow-shocks associated to high-velocity bullets. Furthermore, a preliminary analysis of narrow-band images of the knots suggests that [N II] peaks farther away from the central star than [O III] (Miranda et al. 2012b). The enhanced [N II] emission in the knots seems to imply shock-excitation, whereas the strong [O III] emission rather points to irradiation from the central star. A comprehensive analysis of the emission spectrum of the knots is crucial to determine the excitation mechanism, as done by, e.g., Riera et al. (2006) for Hen 3-1475 and Guerrero et al. (2008) for IC 4634.

The physical structure of its main nebular shell is also largely unknown. Narrow-band [N II] image (Miranda et al. 2012a) reveals a complex morphology for its innermost regions, which adds to the peculiar velocity field revealed by kinematical studies (Sabbadin, Bianchini & Hamzaoglu 1983; Sabbadin, Cappellaro & Turatto 1987). Similarly, the kinematical structure of the faint bipolar lobes is completely unknown. The relatively large He/H and N/O abundance ratios of the bright inner regions of Hu 1-2 qualify it to be Type I PN (Peimbert & Torres-Peimbert 1987), but detailed abundance analyses of the same nebular regions (Pottasch et al. 2003; Hyung, Pottasch & Feibelman 2004) found that abundances of the  $\alpha$  elements (oxygen, neon, sulfur and argon) are much lower than those in most other Galactic PNe. This peculiar abundance pattern may shed light on the origin and evolution of Hu 1-2, but a spatially-resolved study of the physical conditions, chemical abundances, and excitation mechanisms is lacking.

In this paper we present high spatial resolution narrow-band optical and near-infrared images and high- and intermediate-dispersion long-slit optical spectra of Hu 1-2. These data have allowed us to carry out a complete analysis of its spatio-kinematical properties and physical conditions, abundances, and excitation mechanisms. Particular emphasis is made in the investigation of the properties of the collimated outflows in Hu 1-2.

**Table 1.** Observing log of imaging.

Telescope	Instrument	Filter	$\lambda_c$	$\Delta\lambda$	Exp. Time (s)
NOT	ALFOSC	[O III]	5007 Å	30 Å	600
		H $\alpha$	6567 Å	8 Å	600
		[N II]	6588 Å	9 Å	900
TNG	NICS	Br $\gamma$	2.169 $\mu\text{m}$	0.035 $\mu\text{m}$	1200
		H $_2$	2.122 $\mu\text{m}$	0.032 $\mu\text{m}$	1200
		$K_c$	2.275 $\mu\text{m}$	0.039 $\mu\text{m}$	1200

## 2 OBSERVATIONS

### 2.1 Imagery

Narrow-band optical images in the [O III], H $\alpha$ , and [N II] emission lines were acquired on 2008 September 2 using the Andalucía Faint Object Spectrograph and Camera (ALFOSC) on the 2.5m Nordic Optical Telescope (NOT) of the Observatorio del Roque de los Muchachos (ORM) on the island of La Palma (Spain). The characteristics of the narrow-band filters used in these observations (central wavelength  $\lambda_c$  and bandwidth  $\Delta\lambda$ ) are summarized in Table 1. An EEV 2k $\times$ 2k CCD was used as detector, yielding a plate scale of  $0''.184 \text{ pixel}^{-1}$  and a field of view (FoV) of  $6'.3 \times 6'.3$ .

Two images in each filter were obtained with a small dithering between them to eliminate cosmic rays and reduce cosmetic defects of the CCD. The images were bias-subtracted, flat-fielded by twilight flats, and combined using standard IRAF<sup>1</sup> V2.14.1 routines. The spatial resolution of the final images, as derived from the FWHM of stars in FoV is  $0''.7$ .

The three images were then background-subtracted and flux-calibrated using the H $\alpha$ , [N II]  $\lambda 6583$  and [O III]  $\lambda 5007$  line fluxes measured in the intermediate-dispersion spectrum that will be presented in Section 2.2. The individual flux-calibrated narrow-band images of Hu 1-2 are presented in Figure 1, whereas a color-composite picture is displayed in Figure 2. In Figure 3 we present a close-up of the [N II] emission from the inner region of Hu 1-2.

Narrow-band, near-infrared (IR) images were obtained on 2004 July 11 with the 3.5m Telescope Nazionale Galileo (TNG) also at the ORM. The Near-Infrared Camera and Spectrograph (NICS) was used with a 1024 $\times$ 1024 Rockwell HgCdTe array. The spatial scale is  $0''.13 \text{ pixel}^{-1}$  and the FoV is  $2'.2 \times 2'.2$ . The images were obtained through Br $\gamma$ , H $_2$  and continuum ( $K_c$ ) filters whose central wavelengths and bandwidths are given in Table 1. The images were reduced with the MIDAS<sup>2</sup> package following standard procedures for near-IR image reduction. The spatial resolution of the final images, as derived from the FWHM of field stars in the FoV, is  $0''.75$ . Figure 4 presents the three near-IR images.

### 2.2 Intermediate-dispersion spectroscopy

Intermediate-dispersion spectra of Hu 1-2 were obtained on 2011 October 9, using the ALBIREO spectrograph at the 1.5m telescope

<sup>1</sup> IRAF, the Image Reduction and Analysis Facility, is distributed by the National Optical Astronomy Observatory, which is operated by the Association of Universities for Research in Astronomy under cooperative agreement with the National Science Foundation.

<sup>2</sup> MIDAS is developed and distributed by the European Southern Observatory.

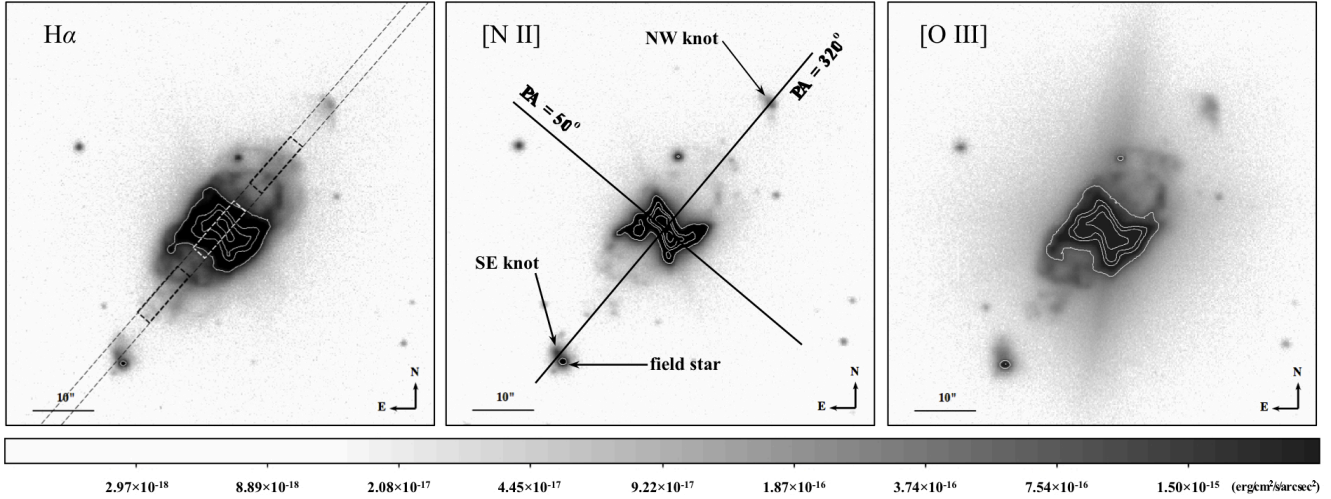


**Figure 1.** Nordic Optical Telescope (NOT) ALFOSC flux-calibrated grey-scale images of Hu 1-2 in  $H\alpha$  (left),  $[N II]$  (middle) and  $[O III]$  (right). The  $2''.5$ -wide long slit along  $PA \approx 320^\circ$  used for the intermediate-dispersion spectroscopy (see Section 2.2) was placed across the northwest (NW) and southeast (SE) knots as indicated by long-dashed lines in the  $H\alpha$  image, where the slit apertures used to extract 1-D spectra for the inner and outer regions are indicated by the heavy white and black dashed boxes ( $10''$  each in length), respectively. The NW and SE knots, as well as a field star partially superimposed on the SE knot, are indicated in the  $[N II]$  image, where the two slit positions used for high-dispersion spectroscopy (see Section 2.3) are indicated with two black lines (slit width not to scale). The “spikes” along the north-south direction in the  $[O III]$  image are stray light due to the very strong  $[O III]$  emission from the inner region of Hu 1-2. Images are scaled to the same level and the grey levels are in logarithm. The white contours over-plotted in the central regions correspond to  $2.5 \times 10^{-14}$ ,  $1.0 \times 10^{-14}$ ,  $5.0 \times 10^{-15}$ , and  $1.0 \times 10^{-15} \text{ erg cm}^{-2} \text{ s}^{-1} \text{ arcsec}^{-2}$ . The color bar below shows the grey scale in surface brightness (in  $\text{erg cm}^{-2} \text{ s}^{-1} \text{ arcsec}^{-2}$ ).

of the Observatorio de Sierra Nevada (OSN), Granada, Spain. A Marconi  $2048 \times 2048$  CCD was used as a detector, in conjunction with the  $400 \text{ lines mm}^{-1}$  grating #4 blazed at  $5500 \text{ \AA}$ . The slit length was  $\sim 6'$  and its width was set at  $50 \mu\text{m}$  ( $\equiv 2''.5$ ). A  $2 \times 2$  binning in the detector was used, implying plate and spectral scales of  $1''.53 \text{ pixel}^{-1}$  and  $3.54 \text{ \AA pixel}^{-1}$ , respectively. The spectral resolution was  $\sim 4.7 \text{ \AA}$ , and the wavelength uncertainty  $\sim 1 \text{ \AA}$ . The spectral coverage is  $3570\text{--}7200 \text{ \AA}$ . The seeing, as determined from the FWHM of the continuum of field stars covered by the slit, was  $\sim 3''$ . As illustrated in Figure 1-left, the slit was aligned along a position angle (PA) of  $320^\circ$ , i.e., along the major nebular axis and through the bipolar knots.

Three 60 s and six 300 s exposures were obtained to secure information both from the bright and faint emission lines in this nebula; indeed, the bright  $[O III] \lambda 5007$  emission line was found to saturate in the central regions of the nebula in the long exposures. All the spectra were bias-subtracted, flat-fielded, wavelength and flux calibrated, following standard procedures using IRAF. Spectra of the spectrophotometric standard star Feige 115 acquired on the same night were used to carry out the flux calibration.

### 2.3 High-dispersion spectroscopy

Two high-dispersion, long-slit spectra of Hu 1-2 were obtained in 2004 June with IACUB<sup>3</sup> on the 2.5m NOT at ORM. The slit positions, oriented at PAs  $50^\circ$  and  $320^\circ$ , are shown in Figure 1-middle. The long-slit spectra at  $PA 320^\circ$  was already presented by Miranda et al. (2012a) in the analysis of the kinematics of the bipolar knots. The  $H\alpha$  and  $[N II] \lambda\lambda 6548, 6583$  emission lines were observed

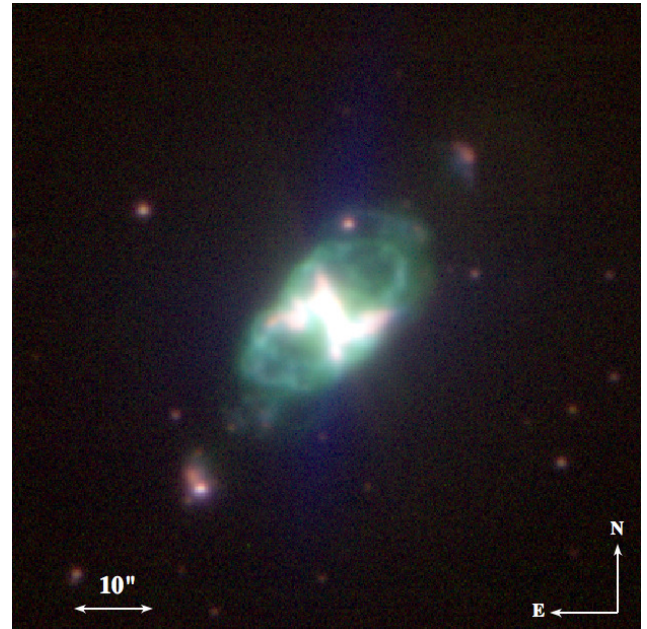


**Figure 2.** Color-composite picture of Hu 1-2 in the  $[N II]$  (red),  $H\alpha$  (green), and  $[O III]$  (blue) emission lines. All intensities are displayed in logarithmic scale. A field star is partially superimposed on the southeast (SE) knot.

with a slit width of  $0''.65$  for an exposure of 900 s. The spectral resolution (FWHM) is  $8 \text{ km s}^{-1}$ , and the spatial resolution is  $\simeq 1''$ . See Miranda et al. (2012a) for a detailed description of these observations.

<sup>3</sup> The IACUB uncrossed echelle spectrograph was built in a collaboration between the Instituto de Astrofísica de Canarias (IAC) and Queen's University of Belfast.

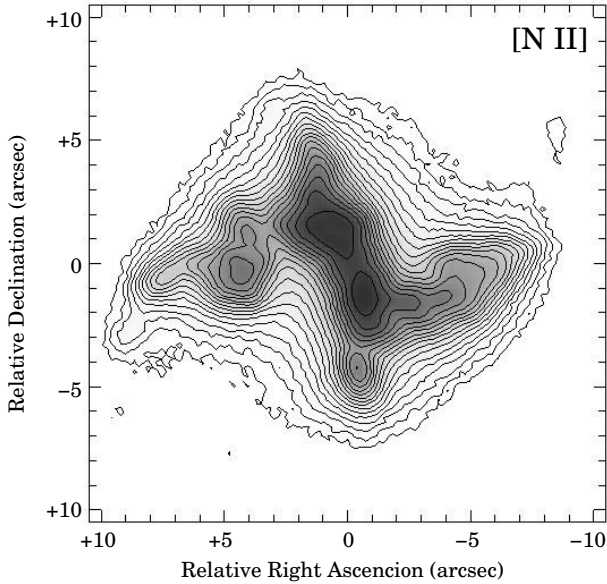


**Figure 3.** Grey-scale NOT ALFOSC [N II] narrow-band image of Hu 1-2 over-plotted with contours, showing the complex knotty structure in its central regions. The image is centered on the central star (as can be seen in Figure 4). Grey scale is in logarithm and the contour levels are arbitrary.

### 3 MAIN NEBULA

#### 3.1 Morphology

The optical narrow-band images in Figure 1 show that Hu 1-2 has an elongated elliptical or slightly bipolar main nebula with a size of  $\sim 12'' \times 32''$  with the major axis oriented at  $PA \sim 320^\circ$ , and a pair of bipolar knots (NW and SE) located along the main nebular axis, each  $\sim 27''$  away from the central star. As already noted by Miranda et al. (2012a), the SE knot is partially superimposed by a field star and cannot be well studied. At any rate, the high-resolution NOT images reveal that the knots (in particular the NW one) present bow-shock morphology (Figure 1). In the central region of Hu 1-2, there is a bright,  $z$ -shaped structure (hereafter the inner region) with a size of  $\sim 10'' \times 10''$  (Figure 1-middle; see also description below). The bipolar lobes are considerably fainter than the inner region. Moreover, the lobes harbor a noticeable richness of small structures that differ from each other. The NW lobe seems to be composed of two concentric structures, a NW inner lobe and a NW outer lobe, that are better observed in the  $H\alpha$  image. Only part of the NW outer lobe can be recognized in the [O III] image, where it shows a clearly curly morphology, and in the [N II] image, where the [N II] emission is mainly detected in a couple of very compact regions. A SE counterpart of the NW inner lobe can be recognized, also exhibiting a remarkable curly structure in the [O III] image. No SE counterpart of the NW outer lobe can be identified. Instead, several knots are observed in the [O III] image, that are oriented along (or close to) the main nebular axis. Faint [N II] emission is detected at the leading head of these knots.

A close inspection of the inner region of Hu 1-2 in the [N II] image reveals a peculiar structure, as shown in Figure 3. It shows an arc-shaped central “bar” with a size  $\simeq 6''$  oriented at  $PA \sim 30^\circ$  that contains two bright knots separated by  $\simeq 2''.8$ . There is enhanced emission and/or knots on either end of the bar that seem to trace the edges of bipolar lobes towards the east and west. As a whole, the inner region of Hu 1-2 exhibits a remarkable point-symmetric

structure. It is worth noting that none of the point-symmetric pairs of knots is oriented along the major nebular axis. It is tantalizing to interpret the inner region as a broken equatorial torus, but we have to admit that such a torus would be broken in a very point-symmetric manner. The kinematics of this region, to be described in Section 3.2, is less compatible with that expected from a simple ring-like equatorial torus.

The optical images (Figures 1 and 2) show that [N II] emission is enhanced in the knots and in the inner region while the bipolar lobes (hereafter the outer region) are dominated by the  $H\alpha$  line emission. The strongest [O III] emission comes from both the main nebula and regions behind the head of the knots facing toward the central star.

The point-symmetric inner region is also enhanced in the near-IR emission, as shown in Figure 4, where it presents a very similar morphology to that observed in the optical ones. In addition, faint emission from the bipolar lobes can be recognized in the  $Br\gamma$  filter. The  $H_2$  emission is faint, but definitely present in the NW knot and, possibly, also in the SE counterpart. We have tried to subtract the continuum image from the emission-line images (the subtracted images are not shown here), and found that  $Br\gamma$  emission is present in the inner region and bipolar lobes whereas in the case of  $H_2$ , no satisfactory subtraction was achieved; nevertheless, the presence of  $H_2$  emission in the inner region is doubtful as the emission in the  $H_2$  image can be attributed to continuum emission. Finally we note that both the  $K_c$  and  $H_2$  images show a faint point-like source at the center of the inner region (Figure 4), which could be the central star of Hu 1-2. This point-like source is not well observed in the  $Br\gamma$  image probably due to the relatively stronger line emission. In all three near-IR filters, we observed an emission feature located towards the SW of the central point-like source (better seen in Figure 4-right). A comparison between the NOT ALFOSC [N II] and TNG NICS  $K_c$  images shows that the SW feature in the  $K_c$  image is associated with the SW [N II] knot in the central bar. The  $K_c$  knot peaks closer to the central star by  $\sim 0''.3$ , suggesting that it corresponds to ionized material with higher excitation than the [N II] line.

#### 3.2 Kinematics

The grey-scale position-velocity (PV) maps of the  $H\alpha$  and [N II]  $\lambda 6583$  emission lines derived from the high-resolution, long-slit spectra at  $PA 50^\circ$  and  $320^\circ$  are shown in Figure 5. The PV map of the He II  $\lambda 6560$  emission line is close to that of  $H\alpha$ . The PV map of the [N II] line at  $PA 320^\circ$  was already presented by Miranda et al. (2012a, Figure 2 therein), who focused on the emission features associated with the bipolar knots. We examine in detail the kinematical structure of the main nebula instead. In the following, radial velocities will be quoted with respect to the heliocentric systemic velocity of  $-3.3 \text{ km s}^{-1}$  for Hu 1-2 that we deduced from our high-dispersion spectra (see below).

The [N II] PV map at  $PA=320^\circ$  shows two compact features at  $\simeq 0''.5$  from the center with radial velocities  $\pm 38 \text{ km s}^{-1}$ , with the feature at  $PA 320^\circ$  being redshifted. In the PV map at  $PA 50^\circ$ , the emission features are more elongated along the slit ( $\simeq 10''$ ), and present point-symmetric, arc-like shapes, with the NE feature redshifted and the SW one blueshifted. The emission peaks in these features are located  $\simeq 1''.9$  from the center and their radial velocity amounts to  $\pm 30 \text{ km s}^{-1}$ . At larger distances from the center, the radial velocity in the features remains approximately constant; at smaller distances the radial velocity increases up to  $\simeq -48 \text{ km s}^{-1}$  at  $\simeq 0''.3$  from the center in the blueshifted feature and up to  $\simeq +43$

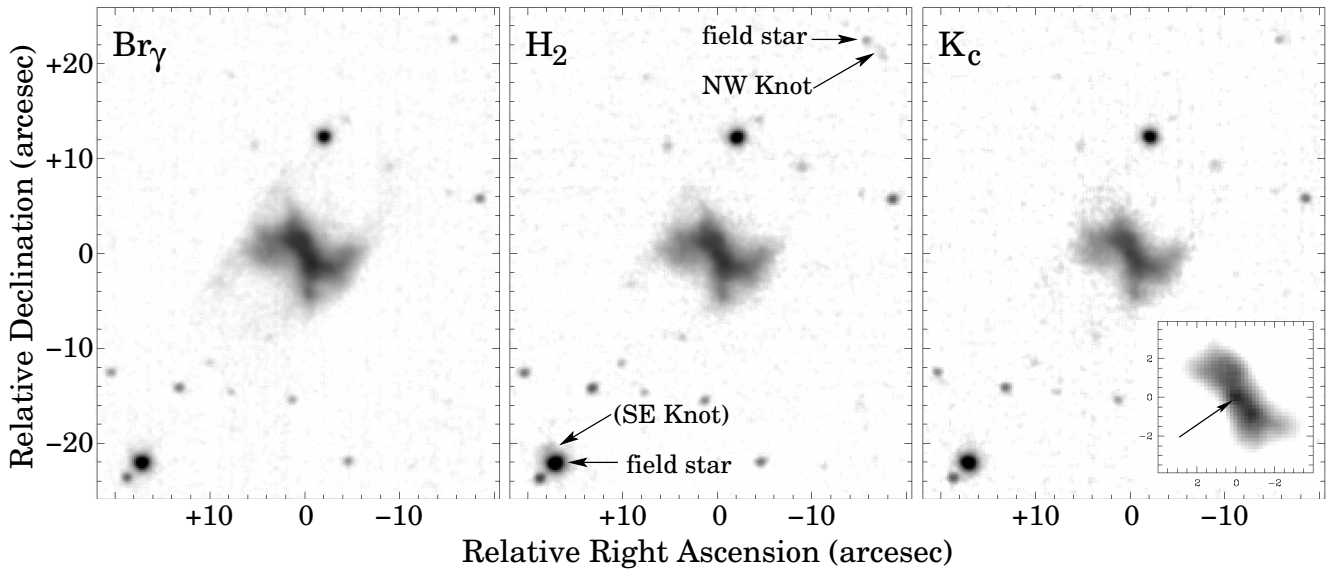


**Figure 4.** Grey-scale reproductions of the narrow-band, near-IR images of Hu 1-2. Grey levels are logarithmic and have been chosen to emphasize the main nebular structures detected. The NW knot, faint emission possibly from the SE knot, and two field stars are indicated. The inset in the  $K_c$  image (right panel) shows the inner  $4'' \times 4''$  central region of Hu 1-2 in linear grey levels. The arrow indicates a point-like source at the nebula's center that may correspond to the central star.

$\text{km s}^{-1}$  at  $1''.5\text{--}3''.2$  from the center in the redshifted feature. This morphology in the PV diagram indicates a rotation of the torus. If the inner structure is/was indeed a ring (or torus), then it could have been distorted by some agent such as several bipolar ejections along different directions, as suggested by the point-symmetry of the bright regions. If this is the case, the kinematics cannot be interpreted easily. An isolated knot is also observed at  $-43 \text{ km s}^{-1}$  and  $2''.5$  (Figure 5), which reflects the complexity of the inner structure.

These [N II] features are generally consistent with the brightest features in the  $\text{H}\alpha$  PV maps. The arc shape of the [N II] features in the PV map at PA  $50^\circ$  can also be recognized in  $\text{H}\alpha$  with radial velocities about  $5 \text{ km s}^{-1}$  lower than those measured in the [N II] emission line. In the  $\text{H}\alpha$  PV map, these features are embedded or superimposed on a broad and faint  $\text{H}\alpha$  component that extends to  $\simeq 12''$  and  $\simeq 130 \text{ km s}^{-1}$  in radial velocity. The broad  $\text{H}\alpha$  emission is mostly symmetrical with respect to the velocity axes. At PA  $320^\circ$  the extended  $\text{H}\alpha$  emission is observed up to a distance of  $12''$  on both sides of the center. This emission corresponds to the elliptical/bipolar lobes of the nebula. Although the emission is very faint in the PV maps, the observed kinematics appears compatible with that expected from an hour-glass nebula. The total spatial extent of the  $\text{H}\alpha$  emission detected in the PV maps ( $12'' \times 24''$ ) coincides very well with the spatial extent of the main nebula observed in direct images.

Two bright features are detected in the He II emission line at both PAs. Their radial velocity separation amounts to  $\simeq 33 \text{ km s}^{-1}$ , while their spatial separation is  $\simeq 1''.7$  at PA  $50^\circ$  (where they present a slight spatial elongation) and  $\simeq 0''.4$  at PA  $320^\circ$  (Figure 5). The brightest features in each of the three emission lines and their spatio-kinematical properties indicate that they probably trace a unique structure that is related to the bright inner region of Hu 1-2.

It has been shown that differing the systemic velocities ( $v_{\text{sys}}$ ) of the main nebular shell and collimated outflows can be associated to the presence of a binary central star (e.g., Miranda et al. 2001). Using our high-dispersion spectra of Hu 1-2, we measured the he-

liocentric systemic velocities of the main nebula and the knots:  $v_{\text{sys}}(\text{nebula}) = -3.3 \pm 1.7 \text{ km s}^{-1}$ , and  $v_{\text{sys}}(\text{knot}) = +1.4 \pm 2.5 \text{ km s}^{-1}$ . These two systemic velocities agree within the errors and, therefore, they cannot confirm whether a binary central star exist or not. We note that our measurement of the nebular systemic velocity are consistent, but not completely coincident, with previous measurements:  $-9.0 \pm 8.1 \text{ km s}^{-1}$  (Schneider et al. 1983) and  $+9.0 \pm 4.3 \text{ km s}^{-1}$  (Durand et al. 1998). These differences most likely reflect the complex kinematical structure of the main nebular shell of Hu 1-2, which makes difficult a precise estimate of the systemic velocity based on spatially unresolved observations.

### 3.3 Spatio-kinematical model

The  $\text{H}\alpha$  PV map at PA  $320^\circ$  is similar to that found in other bipolar nebula (e.g., Kn 26; Guerrero et al. 2013) suggesting bipolar expansion. We have adopted the prescription by Solf & Ulrich (1985) to model a bipolar outflow, where the radial velocity ( $v_r$ ) at a latitude angle ( $\phi$ ) above the equatorial plane is given by

$$v_r(\phi) = v_p + (v_p - v_e) \times \sin^\gamma(\phi) \quad (1)$$

where  $v_p$  and  $v_e$  are the polar and equatorial velocities, respectively, and  $\gamma$  is a parameter to fit the specific shape of the hour-glass. We note that the PV map suggests a small inclination angle with respect to the plane of the sky. Figure 6 shows three hour-glass models at inclination angles of  $10^\circ$ ,  $5^\circ$ , and  $0^\circ$ , each assuming that  $v_p$  and  $v_e$  are  $150$  and  $30 \text{ km s}^{-1}$ , respectively, and a polar radius ( $R_p$ ) of  $12''.5$ . By varying the parameter  $\gamma$  we obtained the best fit model for the PV map.

It is clear from Figure 6 that no ideal representation of the kinematics can be reached. Whereas one particular set of parameters explains the observed kinematics of a given region (e.g., the front side of the SE lobe and the rear side of the NW lobe), other parameters are needed to reproduce the observed kinematics of other nebular regions (e.g., the rear side of the SE lobe and the front side of the NW lobe). This is not surprising because the images



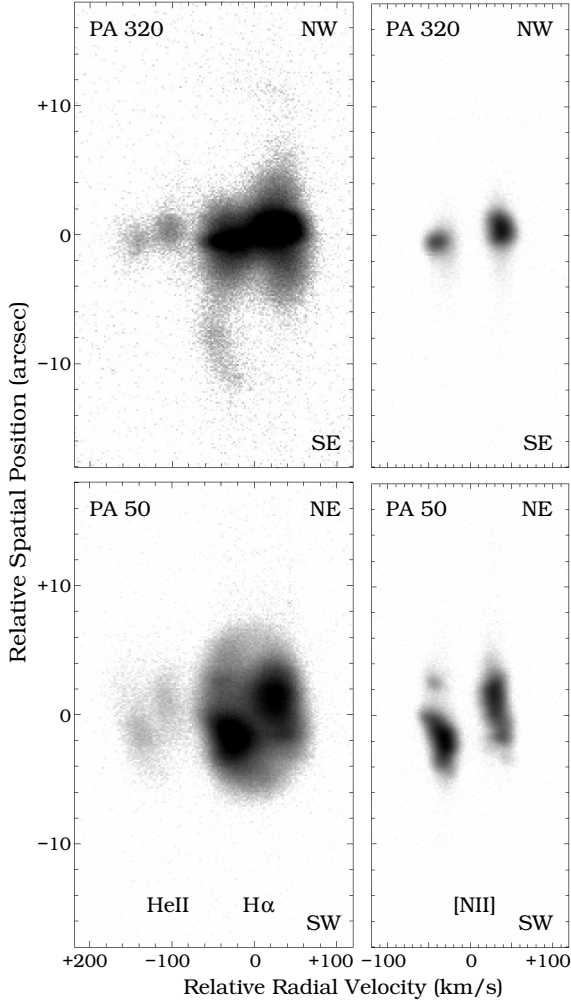


**Figure 5.** Grey-scale PV maps of the He II and H $\alpha$  lines (left) and the [N II] line (right). In the left panels, the two weak features bluewards of H $\alpha$  belong to the He II  $\lambda$ 6560 line. The slit PA = 320° and 50° (see Figure 1-middle) are shown in the upper and lower panels, respectively.

already suggest noticeable morphological differences between the two lobes, and these are reflected into differences in their intrinsic kinematics. From our analysis we conclude that a reasonable upper limit for the inclination angle of the polar axis is 10° and an approximate value for the polar expansion velocity is 150 km s<sup>-1</sup>. Assuming a lower limit of 3.5 kpc for the distance to Hu 1-2 (Miranda et al. 2012a), we derived a lower limit  $\simeq 1100$  yr for the kinematical age of the bipolar lobes, which is consistent with the value of  $1375^{+590}_{-320}$  yr obtained for the bipolar knots (Miranda et al. 2012a).

The [N II] features in the PV maps could be due to a tilted torus (or ring-like structure). If we assume a diameter of 10'' for the equator and a projection of 1'' due to tilt, an inclination angle  $\simeq 6^\circ$  is obtained for the plane of the ring with respect to the line of sight. This value is compatible with the inclination angle of the bipolar lobes. However, the observed kinematics strengthens the idea that the inner regions of Hu 1-2 is difficult to be interpreted as a simple equatorial torus. In particular, for a torus oriented at PA  $\simeq 50^\circ$  and seen almost edge on, a long-slit spectrum along PA  $\simeq 50^\circ$  should show a velocity ellipse with maximum splitting at the center and decreasing towards the edges of the torus. The PV map at PA  $\simeq 50^\circ$  (Figure 5) shows a very different structure. A possible inter-

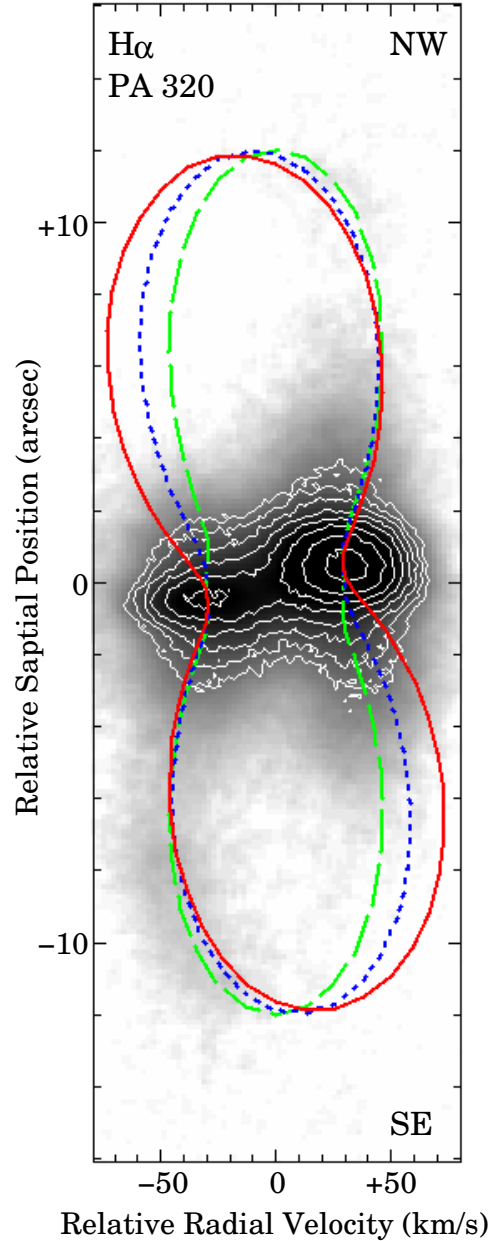


**Figure 6.** Grey-scale PV map of the H $\alpha$  emission line at PA = 320°. A smoothing with a 3 $\times$ 3 pixel box has been applied to the original PV map (see also Figure 5). The over-plotted white contours define the position of the two emission maxima. Also over-plotted are three hour-glass models ( $v_p = 150$  km s<sup>-1</sup>,  $R_p = 12''/5$ ) with different inclination angles of the polar axis with respect to the plane of the sky,  $\theta$ , and the model parameter  $\gamma$  (see Equation 1):  $\theta = 10^\circ$  and  $\gamma = 2.5$  (red solid line),  $\theta = 5^\circ$  and  $\gamma = 3.5$  (blue dotted line), and  $\theta = 0^\circ$  and  $\gamma = 4.5$  (green dashed line).

pretation for the inner region is that a series of bipolar ejections at different directions have been involved in its formation, distorting a previous, more defined structure.

#### 4 SPECTRAL ANALYSIS

One-dimensional (1-D) spectra of the bright inner region, the bipolar lobes, and the bipolar knots were extracted with the spatial ex-

**Table 2.** Emission lines detected in the inner region, outer region, and NW knot of Hu 1-2. The observed fluxes and the extinction corrected intensities are all normalized to  $H\beta = 100$ . The colon “:” indicates a large uncertainty in the line intensity. Logarithm of the total observed  $H\beta$  fluxes measured from the 1-D spectra extracted from the slit apertures shown in Figure 1-*left* are given at the bottom of the table.

$\lambda_{\text{obs}}$ (Å)	Inner Region		Outer Region		NW Knot		Ion	Mult.	$\lambda_{\text{lab}}$ (Å)	Lower	Upper	$g_1$	$g_2$
	$F(\lambda)$	$I(\lambda)$	$F(\lambda)$	$I(\lambda)$	$F(\lambda)$	$I(\lambda)$							
3726.2 <sup>a</sup>	47.8	75.2±2.5	14.7	23.1±1.5	347	545±34	[O II]		3727	2p <sup>3</sup> 4S <sup>o</sup>	2p <sup>3</sup> 2D <sup>o</sup>	4	4
3749.5	2.11	3.30±0.35					H I	H12	3750	2p <sup>2</sup> P <sup>o</sup>	12d <sup>2</sup> D	8	
3757.8 <sup>b</sup>	1.87	2.91±0.32	4.65	7.2±0.8			O III	V2	3757	3s <sup>3</sup> P <sup>o</sup>	3p <sup>3</sup> D	1	3
3769.9	2.89	4.5±0.5					H I	H11	3770	2p <sup>2</sup> P <sup>o</sup>	11d <sup>2</sup> D	8	
3797.1	3.78	5.8±0.6					H I	H10	3798	2p <sup>2</sup> P <sup>o</sup>	10d <sup>2</sup> D	8	
3815.9	1.08	1.7±0.4	12.9	20±5			He II		3813	4f <sup>2</sup> F <sup>o</sup>	19g <sup>2</sup> G	32	
3834.4	5.19	7.9±0.6					H I	H9	3835	2p <sup>2</sup> P <sup>o</sup>	9d <sup>2</sup> D	8	
3868.0	50.8	76.5±1.3	29.5	44.4±1.8			[Ne III]		3868	2p <sup>4</sup> 3P	2p <sup>4</sup> 1D	5	5
3888.0 <sup>c</sup>	12.3	18.5±0.7	12.6	18.9±0.7			H I	H8	3889	2p <sup>2</sup> P <sup>o</sup>	8d <sup>2</sup> D	8	
3922.0	0.52	0.78±0.21					He II		3923	4f <sup>2</sup> F <sup>o</sup>	15g <sup>2</sup> G	32	
3967.5 <sup>d</sup>	26.5	38.6±1.2	18.7	27.3±1.8	80.6	117±8	[Ne III]		3967	2p <sup>4</sup> 3P	2p <sup>4</sup> 1D	3	5
4024.8	1.68	2.40±0.35					He I		4024	2p <sup>1</sup> P <sup>o</sup>	7s <sup>1</sup> S	1	3
4067.9	3.67	5.1±0.5					[S II]		4068	3p <sup>3</sup> 4S <sup>o</sup>	2p <sup>3</sup> 2P <sup>o</sup>	4	4
4100.4 <sup>e</sup>	18.0	24.9±0.46	17.6	24.3±1.0	38.0	52.5±2.2	H I	H6	4101	2p <sup>2</sup> P <sup>o</sup>	6d <sup>2</sup> D	8	72
4143.9	0.211	0.29±0.13					He I	V53	4144	2p <sup>1</sup> P <sup>o</sup>	6d <sup>2</sup> D	3	5
4198.2	1.26	1.67±0.25					He II		4200	4f <sup>2</sup> F <sup>o</sup>	11g <sup>2</sup> G	32	
4226.7	0.24	0.32±0.10					[Fe V]		4227	3d <sup>4</sup> 5D	3d <sup>4</sup> 3H	9	9
4340.0	38.1	47.5±1.2	30.3	37.7±1.9	34.2	42.6±2.3	H I	H5	4340	2p <sup>2</sup> P <sup>o</sup>	5d <sup>2</sup> D	8	50
4362.5	14.6	18.0±0.6	7.82	9.6±0.6			[O III]		4363	2p <sup>2</sup> 1D	2p <sup>2</sup> 1S	5	1
4386.6	0.36	0.44±0.10					He I	V15	4388	2p <sup>1</sup> P <sup>o</sup>	5d <sup>1</sup> D	3	5
4470.9	2.31	2.72±0.21					He I	V14	4471	2p <sup>3</sup> P <sup>o</sup>	4d <sup>3</sup> D	9	15
4541.2	2.94	3.35±0.19					He II		4541	4f <sup>2</sup> F <sup>o</sup>	9g <sup>2</sup> G	32	
4640.8	1.92	2.1±0.8					N III	V2	4641	3p <sup>2</sup> P <sup>o</sup>	3d <sup>2</sup> D	4	6
4685.6	88.6	95.0±2.1	117	126±6	132	142±6	He II		4686	3d <sup>2</sup> D	4f <sup>2</sup> F <sup>o</sup>	18	3
4711.3	8.25	8.8±0.8	7.76	8.2±1.1			[Ar IV]		4711	3p <sup>3</sup> 4S <sup>o</sup>	3p <sup>3</sup> 2D <sup>o</sup>	4	6
4725.6	1.84	1.9±0.7					[Ne IV]		4724	2p <sup>3</sup> 2D <sup>o</sup>	2p <sup>3</sup> 2P <sup>o</sup>	4	6
4740.2	5.80	6.09±0.25	5.83	6.1±0.5			[Ar IV]		4740	3p <sup>3</sup> 4S <sup>o</sup>	3p <sup>3</sup> 2D <sup>o</sup>	4	4
4861.6 <sup>f</sup>	100	100	100	100	100	100	H I	H4	4861	2p <sup>2</sup> P <sup>o</sup>	4d <sup>2</sup> D	8	32
4921.8	0.70	0.7±0.5					He I	V48	4922	2p <sup>1</sup> P <sup>o</sup>	4d <sup>1</sup> D	3	5
4959.3	252	243±3	168	162±2	408.31	394±8	[O III]		4959	2p <sup>2</sup> 3P	2p <sup>2</sup> 1D	3	5
5007.0	775	735±5	516	489±4	1109.88	1053±11	[O III]		5007	2p <sup>2</sup> 3P	2p <sup>2</sup> 1D	5	5
5145.5	0.30	0.27:					[Fe VI]		5145	3d <sup>3</sup> 4F	3d <sup>3</sup> 2G	8	8
5176.9	0.25	0.22:					[Fe VI]		5176	3d <sup>3</sup> 4F	3d <sup>3</sup> 2G	10	10
5198.7 <sup>g</sup>	2.02	1.80±0.25					[N I]		5198	2p <sup>3</sup> 4S <sup>o</sup>	2p <sup>3</sup> 2D <sup>o</sup>	4	4
5275.9	0.21	0.18:					[Fe VI]		5278	3d <sup>3</sup> 4F	3d <sup>3</sup> 4P	4	4
5335.6	0.30	0.26:					[Fe VI]		5335	3d <sup>3</sup> 4F	3d <sup>3</sup> 4P	4	2
5412.0	8.71	7.3±0.5	8.09	6.8±0.9			He II		5411	4f <sup>2</sup> F <sup>o</sup>	7g <sup>2</sup> G	32	98
5483.8	0.14	0.11:					[Fe VI]		5485	3d <sup>3</sup> 4F	3d <sup>3</sup> 4P	6	2
5516.4	0.56	0.46±0.14					[Cl III]		5517	3p <sup>3</sup> 4S <sup>o</sup>	3p <sup>3</sup> 2D <sup>o</sup>	4	6
5538.3	0.74	0.60±0.14					[Cl III]		5537	3p <sup>3</sup> 4S <sup>o</sup>	3p <sup>3</sup> 2D <sup>o</sup>	4	4
5630.0	0.14	0.11:					[Fe VI]		5631	3d <sup>3</sup> 4F	3d <sup>3</sup> 4P	8	4
5678.1	0.25	0.20:					[Fe VI]		5677	3d <sup>3</sup> 4F	3d <sup>3</sup> 4P	10	6
5721.4	0.90	0.70±0.17					[Fe VII]		5721	3d <sup>2</sup> 3F	3d <sup>2</sup> 1D	5	5
5755.4	5.73	4.42±0.19					[N II]		5755	2p <sup>2</sup> 1D	2p <sup>2</sup> 1S	5	1
5876.2	12.3	9.2±0.5					He I		5876	2p <sup>3</sup> P <sup>o</sup>	3d <sup>3</sup> D	9	15
6037.9	0.18	0.13±0.14					He II		6036	5g <sup>2</sup> G	21h <sup>2</sup> H <sup>o</sup>	50	
6072.8	0.24	0.18±0.16					He II		6074	5g <sup>2</sup> G	20h <sup>2</sup> H <sup>o</sup>	50	
6086.2	1.61	1.16±0.15					[Fe VII]		6086	3d <sup>2</sup> 3F	3d <sup>2</sup> 1D	7	5
6101.3	0.42	0.30±0.10					[K IV]		6102	3p <sup>4</sup> 3P	3p <sup>4</sup> 1D	5	5
6117.9	0.32	0.23±0.13					He II		6118	5g <sup>2</sup> G	19h <sup>2</sup> H <sup>o</sup>	50	
6169.9	0.31	0.22±0.12					He II		6170	5g <sup>2</sup> G	18h <sup>2</sup> H <sup>o</sup>	50	
6232.5	0.49	0.34±0.14					He II		6234	5g <sup>2</sup> G	17h <sup>2</sup> H <sup>o</sup>	50	
6300.3	8.52	5.89±0.25					[O I]		6300	2p <sup>4</sup> 3P	2p <sup>4</sup> 1D	5	5
6311.8 <sup>h</sup>	5.02	3.47±0.14	4.51	3.11±0.19			[S III]		6312	3p <sup>2</sup> 1D	3p <sup>2</sup> 1S	5	1
6363.6	2.68	1.83±0.11					[O I]		6363	2p <sup>4</sup> 3P	2p <sup>4</sup> 1D	5	3

**Table 2.** Continued.

$\lambda_{\text{obs}}$ (Å)	Inner Region		Outer Region		NW Knot		Ion	Mult.	$\lambda_{\text{lab}}$ (Å)	Lower	Upper	$g_1$	$g_2$
	$F(\lambda)$	$I(\lambda)$	$F(\lambda)$	$I(\lambda)$	$F(\lambda)$	$I(\lambda)$							
6405.5	0.72	0.49±0.11					He II		6406	5g <sup>2</sup> G	15h <sup>2</sup> H <sup>o</sup>	50	
6434.1	2.70	1.82±0.12	2.58	1.74±0.17			[Ar V]		6435	3p <sup>2</sup> <sup>3</sup> P	3p <sup>2</sup> <sup>1</sup> D	3	5
6526.1	0.75	0.50±0.12					[N II]		6527	2p <sup>2</sup> <sup>3</sup> P	2p <sup>2</sup> <sup>1</sup> D	1	5
6547.5	77.1	51±5	23.1	15.2±2.3	219	144±26	[N II]		6548	2p <sup>2</sup> <sup>3</sup> P	2p <sup>2</sup> <sup>1</sup> D	3	5
6561.9	468	339±20	387	255±19	585	385±32	H I		6563	2p <sup>2</sup> P <sup>o</sup>	3d <sup>2</sup> D	8	18
6582.9	248	162±5	69.9	45.8±2.3	540	354±22	[N II]		6583	2p <sup>2</sup> <sup>3</sup> P	2p <sup>2</sup> <sup>1</sup> D	5	5
6678.3 <sup>i</sup>	4.13	2.7±0.4					He I	V46	6678	2p <sup>1</sup> P <sup>o</sup>	3d <sup>1</sup> D	3	5
6715.7	7.51	4.81±0.22	3.58	2.29±0.21			[S II]		6716	2p <sup>3</sup> <sup>4</sup> S <sup>o</sup>	2p <sup>3</sup> <sup>2</sup> D <sup>o</sup>	4	6
6730.5	12.7	8.11±0.25	6.27	4.00±0.25	47.6	30.4±2.4	[S II]		6731	2p <sup>3</sup> <sup>4</sup> S <sup>o</sup>	2p <sup>3</sup> <sup>2</sup> D <sup>o</sup>	4	4
6820.9	0.52	0.33±0.12					[Fe V]		6819	3d <sup>4</sup> <sup>3</sup> P4	3d <sup>4</sup> <sup>1</sup> S4	3	1
6889.8	1.13	0.70±0.14					He II		6891	5g <sup>2</sup> G	12h <sup>2</sup> H <sup>o</sup>	50	
7004.8	6.43	3.90±0.20	3.97	2.41±0.24			[Ar V]		7006	3p <sup>2</sup> <sup>3</sup> P	3p <sup>2</sup> <sup>1</sup> D	5	5
7065.2	7.22	4.33±0.24	4.00	2.40±0.26			He I		7065	2p <sup>3</sup> P <sup>o</sup>	3s <sup>3</sup> S	9	3
$\log F(\text{H}\beta)^j$	-11.85		-13.61		-14.47								

<sup>a</sup> A blend of the [O II]  $\lambda\lambda 3726, 3729$  lines.<sup>b</sup> Blended with the O III  $\lambda 3760$  ( $3s^3P_2^o - 3p^3D_3$ ) line.<sup>c</sup> Blended with the He I  $\lambda 3888$  ( $2s^3S - 3p^3P^o$ ) line.<sup>d</sup> Blended with the H I  $\lambda 3970$  ( $2p^2P^o - 7d^2D$ ) line.<sup>e</sup> Blended with the N III  $\lambda 4103$  ( $3s^2S_{1/2} - 3p^2P_{1/2}^o$ ) line.<sup>f</sup> Blended with He II  $\lambda 4859$  line, whose flux contribution is negligible. The same happens to H $\alpha$ , whose is blended with He II  $\lambda 6560$ . See the text for details.<sup>g</sup> Blended with the [N I]  $\lambda 5200$  ( $2p^3^4S_{3/2} - 2p^3^2D_{5/2}^o$ ) line.<sup>h</sup> Corrected for the flux of the blended He II  $\lambda 6311$  ( $5g^2G - 16h^2H^o$ ) line.<sup>i</sup> Corrected for the flux of the blended He II  $\lambda 6683$  ( $5g^2G - 13h^2H^o$ ) line.<sup>j</sup>  $\text{erg cm}^{-2} \text{s}^{-1}$  in our extracted spectra.

tents shown in the H $\alpha$  image in Figure 1-*left*. The contamination by a background star with absorptions in the hydrogen Balmer lines renders of little use of the spectrum of the SE knot. The 1-D spectra showed scattered light from the bright inner region of the H $\beta$ + [O III] and H $\alpha$ + [N II] lines. As a result, the 1-D spectra displayed a pedestal of emission under the [O III] and H $\alpha$ + [N II] lines. We removed this dispersed light by fitting a long-pass Gaussian profile to the nebular continuum around these lines. After this correction, the [O III]  $\lambda 5007/\lambda 4959$  and [N II]  $\lambda 6583/\lambda 6548$  line ratios measured from the spectra are both close to their theoretical value of  $\sim 3$ . The corrected 1-D spectra are shown in Figure 7. We also integrated total fluxes of the [O III]  $\lambda 5007$ , [N II]  $\lambda 6583$ , and H $\alpha$  emission lines for the main nebula and estimated the surface brightnesses. The brightness values were used to calibrate the ALFOSC narrow-band images of Hu 1-2 (Section 2.1).

#### 4.1 Physical conditions

The 1-D intermediate-dispersion, normalized spectra of the inner region, outer region, and NW knot of Hu 1-2 are shown in Figure 7. Although at intermediate-dispersion, the long slit spectrum of Hu 1-2 presented here proves to be very deep. The signal-to-noise ratio (S/N) of the spectrum of the inner region is particularly high, and thus many weak emission lines with fluxes lower than 1% of H $\beta$  are detected (see Figure 7). The emission lines detected in the spectra of the three regions are compiled in Table 2.

We derived a logarithmic extinction parameter,  $c(\text{H}\beta)$ , of 0.61 in the inner region of Hu 1-2 using the observed H $\alpha$ /H $\beta$  line ratio.

Here the theoretical H $\alpha$ /H $\beta$  line ratio was adopted from Storey & Hummer (1995), assuming an electron temperature of 10 000 K and a density of  $10^4 \text{ cm}^{-3}$ . Our  $c(\text{H}\beta)$  value agrees with 0.60 given by Pottasch et al. (2003; also Hyung, Pottasch & Feibelman 2004), who carried out echelle spectroscopy at the center of Hu 1-2 with a slit entrance  $1''.2 \times 4''$ , i.e., also the inner region of Hu 1-2. Earlier observations by Peimbert & Torres-Peimbert (1987) and Aller & Czyzak (1979) gave an extinction value of 0.64 and 0.61, respectively. The  $c(\text{H}\beta)$  values derived for the outer region and the NW knot are  $\sim 0.40$  and  $0.90$ , respectively. Given the more accurate emission-line measurements for the inner region, we adopted 0.61 as the extinction in all three regions of Hu 1-2, although we cannot totally rule out the possibility that extinction in the NW knot could be higher. The extinction law of Whitford (1958) was used to apply this correction. We found that the use of different extinction laws (e.g., Whitford 1958; Savage & Mathis 1979; Cardelli, Clayton & Mathis 1989) results in differences in the extinction-corrected fluxes of emission lines in the optical range from  $\sim 3700 \text{ \AA}$  to  $7100 \text{ \AA}$  lower than 5%.

The extinction-corrected relative line intensities,  $I(\lambda)$ , together with the estimated errors, are given in Table 2. Errors in the line intensities were estimated from multiple measurements of the observed fluxes, through the almost linear relation between the two quantities,

$$I(\lambda) = 10^{c(\text{H}\beta) f(\lambda)} F(\lambda), \quad (2)$$

where  $f(\lambda)$  is the reddening function, normalized to  $f(\text{H}\beta) = 0$ , adopted from Whitford (1958). Uncertainties in the extinction func-



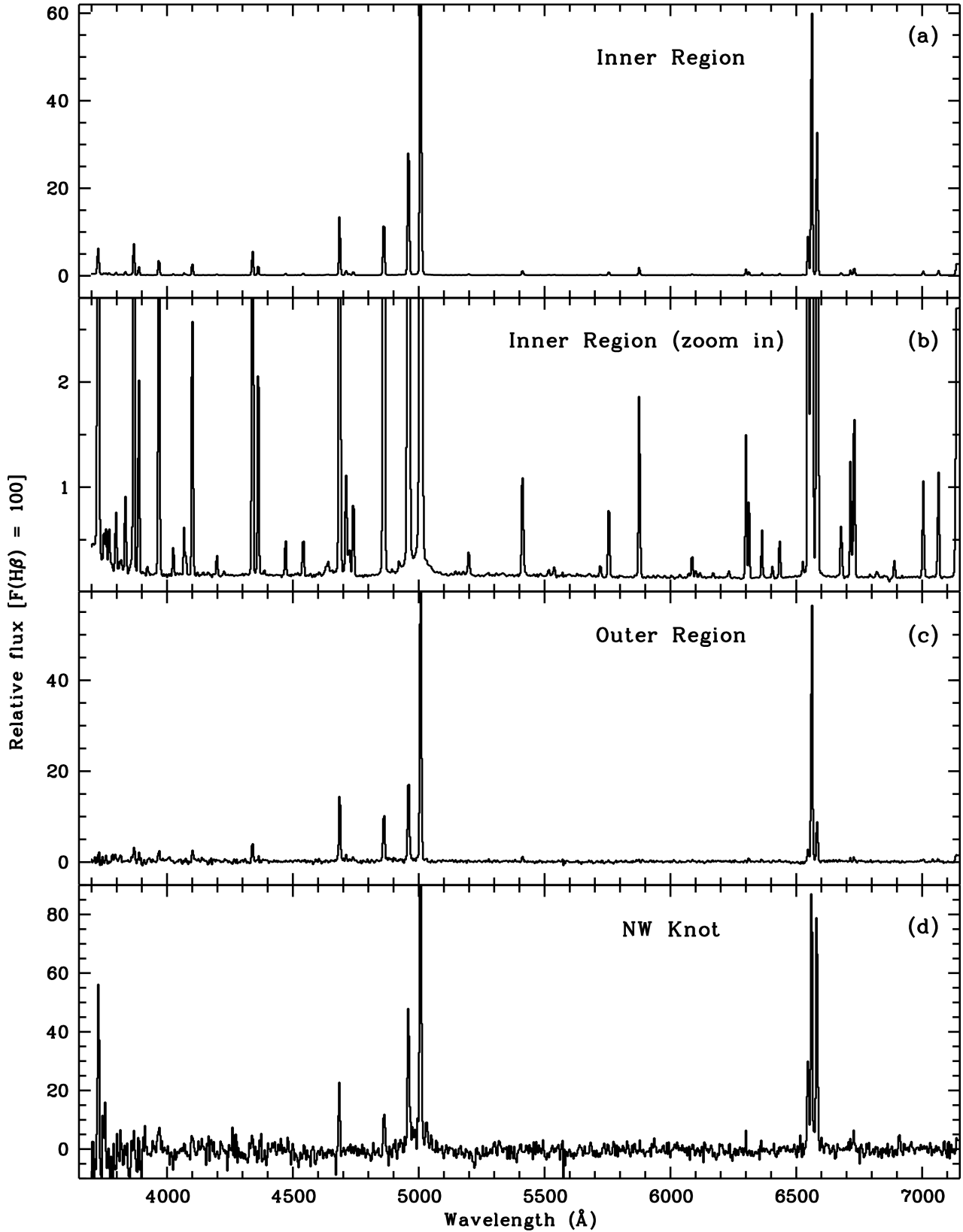


**Figure 7.** One-dimensional intermediate-dispersion optical spectra of the inner region (a and b), outer region (c), and NW knot (d) of Hu 1-2 in the spectral range 3700–7100  $\text{\AA}$ . Panel (b) is a zoom-in view of panel (a) highlighting the weakest emission lines detected in the inner-region spectrum. All spectra have been normalized such that H $\beta$  has an integrated flux of 100. Extinction has not been corrected for. Spectra are scaled to fit the peak intensity of the H $\alpha$  line. Differences in the relative strengths of the [O II] and [N II] lines in the three nebular regions are obvious.

tion are supposed to be negligible, as discussed in the previous paragraph. Flux calibration, which can affect the observed fluxes and consequently the extinction-corrected relative line intensities, was supposed to be accurate.

The [O III]  $\lambda 5007$  line was saturated in the long-exposure (1800 s) spectrum of the inner region, and the flux from the short-exposure (180 s) spectrum was thus used in Table 2. The He II  $\lambda 6560$  ( $4f^2F^\circ - 6g^2G$ ) line is blended with  $H\alpha$ . Using the theoretical line ratios of the hydrogenic ions (Storey & Hummer 1995) and the He II  $\lambda 4686$  line fluxes measured in our spectra, we estimated that the He II  $\lambda 6560$  line contributes  $\sim 3\%$  and  $6\%$  to the total flux of  $H\alpha$  in the inner and outer region of Hu 1-2, respectively. As a consequence, the corrected fluxes of  $H\alpha$  will result in an increase in  $\alpha(H\beta)$  by  $\sim 9\%$  and  $14\%$  in the two regions. That will cause negligible changes in the extinction-corrected line intensities, given that the extinction in Hu 1-2 is low and that the inner-region extinction was adopted for the whole nebula.

The electron temperatures and densities derived for the inner and outer regions using the detected emission lines are presented in Table 3. The [O III] nebular-to-auroral line ratio yielded a temperature of 16 800 K for the inner region, and 15 200 K for the outer region. The [N II] line ratio yielded a temperature of  $\sim 13\,000$  K in the inner region, but the temperature-sensitive  $\lambda 5755$  auroral line was not detected in the outer region. We adopted the above two temperatures for the high- and low-excitation regions in Hu 1-2. An averaged electron density of  $5700\text{ cm}^{-3}$  in the inner region was derived from the [S II]  $\lambda 6716/\lambda 6731$  and [Cl III]  $\lambda 5517/\lambda 5537$  line ratios. It agrees with the density  $5770\text{ cm}^{-3}$  in the outer region, as yielded by the [S II] lines (Table 3). The [Cl III] lines were not detected in the outer region.

## 4.2 Chemical abundances

### 4.2.1 Ionic abundances

Using the electron temperatures defined for the high- and low-excitation zones, we derived the ionic abundances of helium and heavy elements presented in Table 4. The He I effective recombination coefficients used for abundance determination were adopted from Benjamin, Skillman & Smits (1999). For the inner region, we adopted the  $\text{He}^+/\text{H}^+$  abundance ratio derived from the  $\lambda 5876$  line which is the strongest He I line. For the outer region, the  $\text{He}^+/\text{H}^+$  abundance derived from the  $\lambda 7065$  line was adopted. No He I lines were detected in the spectrum of the NW knot.

The  $\text{He}^{2+}/\text{H}^+$  abundance was derived from the He II  $\lambda 4686$  line, which is very strong in all the three regions of Hu 1-2 (Figure 7). The extinction-corrected flux of the He II  $\lambda 4686$  line in the outer region is even higher than that of the  $H\beta$  line by  $\sim 25\%$ , in consistency with the low intensities of the [N II] and [O II] nebular lines. Note, however, that the relative strengths of the [O II]  $\lambda 3727$  (a blend of the  $\lambda\lambda 3726, 3729$  doublet), [N II]  $\lambda\lambda 6548, 6583$ , and He II  $\lambda 4686$  lines in the NW knot are higher than those in the inner and outer regions (Table 2). The He/H abundance is a sum of the  $\text{He}^+/\text{H}^+$  and  $\text{He}^{2+}/\text{H}^+$  ratios and are given in Table 5. The He/H ratio in the inner region (0.144) is slightly lower than that in the outer region (0.159), but a little higher than the NW knot, where no He I line was detected. The absence of He I lines in the NW knot probably indicates that helium in the NW knot is all doubly ionized, although the relatively low S/N's of the spectrum in this region may hinder the detection of the He I lines. Given that measurements of the He I  $\lambda 7065$  line in the outer region of Hu 1-2 have relatively large uncertainties, the He/H abundance in the outer re-

gion is considered to agree with that in the inner region within the errors.

The  $\text{N}^+/\text{H}^+$  abundance derived from the [N II]  $\lambda 6583$  line was adopted for the three regions because measurements of the relatively weaker  $\lambda 6548$  line were much affected by the nearby  $H\alpha$  line. The  $\text{Ne}^{2+}/\text{H}^+$  abundances derived from the [Ne III]  $\lambda 3869$  line were adopted because the [Ne III]  $\lambda 3967$  line was blended with the H I  $\lambda 3970$  line. The [S III]  $\lambda 6312$  line was observed in the inner and outer regions. It was blended with the He II  $\lambda 6311$  ( $5g^2G - 16h^2H^\circ$ ) line, whose flux contribution was estimated from the observed  $\lambda 4686$  line using the hydrogenic atomic model of Storey & Hummer (1995). The corrected flux of the [S III]  $\lambda 6312$  line was used to derive  $\text{S}^{2+}/\text{H}^+$ . The  $\text{Ar}^{3+}/\text{H}^+$  ratio derived from the [Ar IV]  $\lambda 4740$  line was adopted for Hu 1-2, as the  $\lambda 4711$  line was blended with [Ne IV] lines.

The abundance errors following the ionic abundance ratios in Table 4 were mainly propagated from the measurement errors of the extinction-corrected relative line intensities given in Table 2. Both the [O III]  $\lambda 4363$  and the [N II]  $\lambda 5755$  temperature-sensitive auroral lines were well detected in the inner region of Hu 1-2, and the electron temperatures derived from these ions were adopted for all the three regions when calculating ionic abundance ratios (Table 4). Thus the errors in the electron temperature were small (Table 3) and not considered in the ionic abundance calculations.

### 4.2.2 Elemental abundances

The elemental abundances of He, N, O, Ne, S, and Ar in Table 5 were calculated using the ionization correction factor (ICF) method of Kingsburgh & Barlow (1994). No elemental abundances were calculated for the NW knot because the He I line needed for ICF calculations was not detected in this region. The He/H abundance in the inner region of Hu 1-2 derived in this paper is  $\sim 10\%$  higher than that derived by Pottasch et al. (2003) and Hyung, Pottasch & Feibelman (2004), but it agrees with that of Peimbert & Torres-Peimbert (1987) and Peimbert, Luridiana & Torres-Peimbert (1995) within the errors. Meanwhile, the nitrogen abundance derived for the inner region by us is  $\sim 50\%$  higher than that of the outer region, and both are lower than that of previous observations. The oxygen, neon and sulfur abundances in this paper generally agree with those of Pottasch et al. (2003) and Hyung, Pottasch & Feibelman (2004), while our argon abundance is slightly lower. However, uncertainties in abundances were not indicated in the two previous studies. We also notice that the inner-region abundances of N, O, and Ne are higher than those in the outer region.

Errors in the brackets following the total elemental abundances in Table 5 (the first two columns) were estimated mainly based on the errors in the ionic abundances through a simple propagation paradigm. For helium, the error is contributed by uncertainties in the  $\text{He}^+/\text{H}^+$  and  $\text{He}^{2+}/\text{H}^+$  ratios. For heavy elements, the errors can also be introduced by the use of ICFs. This source of error is negligible for oxygen, whose ICF is always close to unity. For other heavy elements, uncertainties introduced by ICFs could be significant. The nitrogen and neon abundances were derived based on the ionic and elemental abundances of oxygen, and thus are reliable. The total sulfur abundance is generally quite uncertain, as usually only the [S II] lines are well observed for this element. Although the [S III]  $\lambda 6312$  line was also detected in the spectrum of Hu 1-2 (Table 2), it arises from an auroral transition ( $3p^2\,^1D_2 - 3p^2\,^1S_0$ ), hence it is particularly temperature sensitive. Besides, the [S III]  $\lambda 6312$  line is also blended with the He II  $\lambda 6311$  ( $5g^2G - 16h^2H^\circ$ ) line. Uncertainties and systematic errors in the ICFs are

**Table 3.** Electron density and temperature of Hu 1-2.

	Inner region	Outer region
$T_e$ (K)		
[O III]	$16\,800 \pm 250$	$15\,200 \pm 400$
[N II]	$13\,000 \pm 400$	
$N_e$ ( $\text{cm}^{-3}$ )		
[S II]	$5100 \pm 1300$	$5770 \pm 2200$
[Cl III]	$6400 \pm 2800$	
[Ar IV]	$3900 \pm 1600$	$3200 \pm 2500$

difficult to define, and thus they were not considered for the error estimate of our object. The actual uncertainties in the elemental abundances of nitrogen, neon, sulfur and argon in Table 5 must be regarded as lower limits of the real abundance uncertainties.

Average abundances of Type I, bulge, and disc PNe as well as the solar abundances are also presented in Table 5 for comparison. The He/H abundances of the inner and outer regions of Hu 1-2 are both higher than 0.14, whereas the N/O ratios of the two regions are both close to 0.9. The He/H and N/O abundance ratios, generally in line with those of Pottasch et al. (2003) and Hyung, Pottasch & Feibelman (2004), indicate that Hu 1-2 belongs to Type I PNe (Peimbert & Torres-Peimbert 1983). On the other hand, the elemental abundances of oxygen, neon, sulfur, and argon in Hu 1-2 are lower than the average abundances of bulge and disc PNe (see Table 5). This difference in abundances is real for the heavy elements, given the uncertainties presented in Table 5 (see the discussion above). Since these four  $\alpha$  elements were not supposed to be produced or depleted in the central star during its evolution<sup>4</sup>, their very low abundances reflect those of the interstellar medium from which the progenitor star of Hu 1-2 formed. Indeed the Ne/H vs. O/H, S/H vs. O/H, and Ar/H vs. O/H abundance patterns of  $\alpha$  elements in Hu 1-2 generally agree with those established for H II regions and blue compact galaxies by Milingo et al. (2010; Figures 1–10 therein). In these figures, the loci of Hu 1-2 are found at the low abundance tail of the samples of Type I PNe (Milingo et al. 2010) and Galactic anticenter PNe (Kwitter et al. 2010).

### 4.3 Could Hu 1-2 be a halo PN?

The abundances of the heavy elements of Hu 1-2 are generally consistent with those of the halo PNe, given their comparatively large abundance scatter as opposed to the disc PNe (Howard, Henry & McCartney 1997). Note, however, that the helium abundances of Hu 1-2 are slightly higher than those of the sample of halo PNe studied by Howard, Henry & McCartney (1997). It is thus pertinent to question whether Hu 1-2 is a halo PN or not.

Halo PNe are characterized by their height above the Galactic plane, their kinematic characteristics, and/or their low metallicity relative to disc PNe. Specifically Peimbert (1990) proposed  $|z| > 0.8$  kpc,  $v_{\text{pec}} > 60 \text{ km s}^{-1}$ , and  $\log(\text{O}/\text{H})+12 < 8.1$  as the criteria for halo PNe, where  $z$  is the distance to the Galactic plane and  $v_{\text{pec}}$  is the peculiar radial velocity, which is the difference between the observed systemic radial velocity of a PN and its cir-

cular radial velocity ( $v_{\text{pec}} = v_{\text{sys}} - v_{\text{circ}}$ ; Peña, Rechy-García & García-Rojas 2013). For Hu 1-2, at a Galactic latitude of  $-8^\circ$ , its distance of  $3.5^{+1.5}_{-0.8}$  kpc (Miranda et al. 2012a) implies a height of  $0.55^{+0.23}_{-0.13}$  kpc over the Galactic plane. Its oxygen abundance is  $\log(\text{O}/\text{H})+12 \sim 8.1$  (see Table 5). Therefore, the oxygen abundance and its distance to the Galactic plane marginally support a halo nature. However, following the formulation by Peña, Rechy-García & García-Rojas (2013, Equation 1 therein), assuming a galactocentric distance of 8.3 kpc for the Sun, adopting a distance of  $3.5^{+1.5}_{-0.8}$  kpc to Hu 1-2, and taking into account the systemic velocity of  $-3.3 \pm 1.7 \text{ km s}^{-1}$  (see Section 3.2), we obtain a peculiar velocity of  $22^{+10}_{-6} \text{ km s}^{-1}$ , which is much lower than required for a PN to belong to the halo. From these results we conclude that most probably Hu 1-2 is not a halo PN.

### 4.4 Excitation mechanism of the outer knots

The  $\text{H}\alpha$ , [N II] and [O III] composite picture of Hu 1-2 (Figure 2) shows two bipolar knots at a distance  $\sim 27''$  from the central source. The ionization and excitation conditions of these knots are studied in detail in this section using our narrow-band images and long-slit intermediate-dispersion spectroscopy. Since the SE knot is partially superimposed by a field star, our analysis will be mainly based on the NW knot, in which a bow-shock-like structure is otherwise clearly observed.

Figure 8 shows the NOT ALFOSC  $\text{H}\alpha$ , [O III]  $\lambda 5007$ , and [N II]  $\lambda 6583$  surface brightness distributions (or 1-D profiles) projected along the line that connects the NW knot to the center of Hu 1-2. The knot has single-peaked profiles in the three emission lines, but they show notable differences. The  $\text{H}\alpha$  and [O III] emissions extend inward from the head of the bow-shock toward the central source, whereas the distribution of the [N II] line has a single peak. The positions of the peaks in different emission lines also differ; the [N II] peak is the farthest from the central source, the  $\text{H}\alpha$  peak is located at an intermediate distance, and the [O III] peak is the closest to the central source. This same pattern is observed in the bow-shock structures of IC 4634 and NGC 7009 (Raga et al. 2008). The position of the [N II] peak coincides with that of the  $\text{H}_2$  emission, further confirming the small thickness of the shell of low-ionization material. For a distance of 3.5 kpc (Miranda et al. 2012a), the spatial shifts between the  $\text{H}\alpha$  and the [N II] and [O III] peaks are  $\sim 3.5 \times 10^{15} \text{ cm}$  and  $\sim 10^{16} \text{ cm}$ , respectively. These are similar, but somewhat larger, than the shifts of a few times  $10^{15} \text{ cm}$  observed in the outer bow shocks of IC 4634 and NGC 7009.

Figure 9 shows the [O III]/ $\text{H}\alpha$  and [N II]/ $\text{H}\alpha$  ratio maps of the NW knot obtained at each pixel with surface brightness above a threshold value of  $3 \sigma$  from the background. Abrupt changes in these emission line ratios are observed at the position of the  $\text{H}\alpha$  peak. At the leading edge of the bow-shock, the [O III]/ $\text{H}\alpha$  has values of 1.2–1.8. Behind the  $\text{H}\alpha$  peak, the [O III]/ $\text{H}\alpha$  ratio increases up to values 2–3, following the ionization stratification also found in the FLIERs of other PNe (Balick et al. 1998; Riera & Raga 2007). At the head of the bow-shock, where the [O III]/ $\text{H}\alpha$  ratio declines, the [N II] emission is enhanced, with [N II]/ $\text{H}\alpha$  ratios of 2–3, significantly raised from the value  $\leq 0.5$  detected upstream. In short, the NW knot of Hu 1-2 shows a low-excitation [N II]-bright head and a high-excitation [O III]-bright, arc-shaped wing and upstream region.

Our intermediate-dispersion spectroscopy cannot resolve spatially the ionization structure seen in the NOT ALFOSC images, but the use of additional line diagnostic diagrams provides further constraint on the excitation conditions of this knot. The spectrum

<sup>4</sup> This is not the exact case for, at least, the production of neon in some low- and intermediate-mass stars, as analyzed by, e.g., Wang & Liu (2008) and Milingo et al. (2010). Karakas & Lattanzio (2003) also predicted that neon can be produced in a narrow range of stellar mass.

**Table 4.** Ionic abundances<sup>a</sup> derived for the inner region, the outer region, and the NW knot of Hu 1-2.

Ion	$\lambda$ (Å)	$T_e$ <sup>b</sup> (K)	Abundance (X <sup>+</sup> /H <sup>+</sup> )		
			Inner	Outer	Knot
He <sup>+</sup>	4471	10 000	0.052±0.004		
He <sup>+</sup>	5876	10 000	0.060±0.003		
He <sup>+</sup>	7065	10 000	0.087±0.005	0.048±0.005	
He <sup>2+</sup>	4686	16 800	0.084±0.002	0.111±0.005	0.126±0.007
N <sup>+</sup>	5755	13 000	1.70(±0.25)×10 <sup>-5</sup>		
N <sup>+</sup>	6548	13 000	1.66(±0.10)×10 <sup>-5</sup>	4.96(±0.33)×10 <sup>-6</sup>	4.7(±0.4)×10 <sup>-5</sup>
N <sup>+</sup>	6583	13 000	1.79(±0.12)×10 <sup>-5</sup>	5.1(±0.4)×10 <sup>-6</sup>	3.93(±0.30)×10 <sup>-5</sup>
O <sup>+</sup>	3727	13 000	1.92(±0.25)×10 <sup>-5</sup>	5.9(±0.8)×10 <sup>-6</sup>	1.40(±0.12)×10 <sup>-4</sup>
O <sup>2+</sup>	4363	16 800	5.9(±0.5)×10 <sup>-5</sup>	3.16(±0.24)×10 <sup>-5</sup>	
O <sup>2+</sup>	4959	16 800	5.67(±0.24)×10 <sup>-5</sup>	3.78(±0.15)×10 <sup>-5</sup>	9.2(±0.4)×10 <sup>-5</sup>
O <sup>2+</sup>	5007	16 800	5.90(±0.25)×10 <sup>-5</sup>	3.95(±0.18)×10 <sup>-5</sup>	8.5(±0.4)×10 <sup>-5</sup>
Ne <sup>2+</sup>	3869	16 800	1.40(±0.07)×10 <sup>-5</sup>	8.1(±0.6)×10 <sup>-6</sup>	
Ne <sup>2+</sup>	3967	16 800	2.34(±0.14)×10 <sup>-5</sup>	1.66(±0.14)×10 <sup>-5</sup>	7.1(±0.5)×10 <sup>-5</sup>
S <sup>+</sup>	4068	13 000	4.26(±0.35)×10 <sup>-7</sup>		
S <sup>+</sup>	6716	13 000	3.4(±0.4)×10 <sup>-7</sup>	1.62(±0.24)×10 <sup>-7</sup>	
S <sup>+</sup>	6731	13 000	3.28(±0.30)×10 <sup>-7</sup>	1.62(±0.18)×10 <sup>-7</sup>	1.23(±0.14)×10 <sup>-6</sup>
S <sup>2+</sup>	6312	13 000	2.66(±0.35)×10 <sup>-6</sup>	2.26(±0.26)×10 <sup>-6</sup>	
Cl <sup>2+</sup>	5517	13 000	3.7(±0.4)×10 <sup>-8</sup>		
Cl <sup>2+</sup>	5537	13 000	3.77(±0.34)×10 <sup>-8</sup>		
Ar <sup>3+</sup>	4711	16 800	4.8(±0.9)×10 <sup>-7</sup>	4.6(±0.8)×10 <sup>-7</sup>	
Ar <sup>3+</sup>	4740	16 800	3.27(±0.50)×10 <sup>-7</sup>	3.3(±0.6)×10 <sup>-7</sup>	
Ar <sup>4+</sup>	6435	16 800	2.9(±0.4)×10 <sup>-7</sup>	2.8(±0.5)×10 <sup>-7</sup>	
Ar <sup>4+</sup>	7006	16 800	2.31(±0.36)×10 <sup>-7</sup>	1.43(±0.26)×10 <sup>-7</sup>	
K <sup>3+</sup>	6102	16 800	8.1(±2.1)×10 <sup>-9</sup>		

<sup>a</sup> Number ratios relative to hydrogen.<sup>b</sup> The effective recombination coefficients used for the He<sup>+</sup>/H<sup>+</sup> abundance calculations were adopted from Benjamin, Skillman & Smits (1999), where only three temperature cases, 5000 K, 10 000 K, and 20 000 K are presented. We have used the He I atomic data at 10 000 K, which is close to the low-excitation temperature (13 000 K) derived for Hu 1-2.**Table 5.** Elemental abundances derived for the inner and outer regions of Hu 1-2. Abundances from the literature are also presented for comparison.

Ele.	Abundance (X/H)							
	Inner <sup>a</sup>	Outer <sup>b</sup>	Pottasch <sup>c</sup>	Hyung <sup>d</sup>	PTP87 <sup>e</sup>	Bulge <sup>f</sup>	Disk <sup>g</sup>	Solar <sup>h</sup>
He	0.144±0.013	0.159±0.022	0.127	0.130	0.147	0.105	0.115	0.085
N	1.31(±0.22)×10 <sup>-4</sup>	8.7(±1.7)×10 <sup>-5</sup>	1.9×10 <sup>-4</sup>	1.7×10 <sup>-4</sup>	2.2×10 <sup>-4</sup>	1.48×10 <sup>-4</sup>	2.19×10 <sup>-4</sup>	6.76×10 <sup>-5</sup>
O	1.40(±0.20)×10 <sup>-4</sup>	1.01(±0.14)×10 <sup>-4</sup>	1.6×10 <sup>-4</sup>	1.3×10 <sup>-4</sup>	1.6×10 <sup>-4</sup>	3.98×10 <sup>-4</sup>	5.01×10 <sup>-4</sup>	4.90×10 <sup>-4</sup>
Ne	3.3(±0.7)×10 <sup>-5</sup>	2.1(±0.5)×10 <sup>-5</sup>	4.9×10 <sup>-5</sup>	3.0×10 <sup>-5</sup>	3.6×10 <sup>-5</sup>	9.77×10 <sup>-5</sup>	1.35×10 <sup>-4</sup>	8.51×10 <sup>-5</sup>
S	4.2(±1.3)×10 <sup>-6</sup>	4.4(±1.5)×10 <sup>-6</sup>	4.2×10 <sup>-6</sup>	3.5×10 <sup>-6</sup>		6.92×10 <sup>-6</sup>	1.12×10 <sup>-5</sup>	1.32×10 <sup>-5</sup>
Ar	7.8(±2.2)×10 <sup>-7</sup>	8.4(±2.9)×10 <sup>-7</sup>	1.1×10 <sup>-6</sup>	1.1×10 <sup>-6</sup>	7.9×10 <sup>-7</sup>	1.58×10 <sup>-6</sup>	2.19×10 <sup>-6</sup>	2.51×10 <sup>-6</sup>

<sup>a</sup> Elemental abundances of the inner region of Hu 1-2.<sup>b</sup> Elemental abundances of the outer region of Hu 1-2.<sup>c</sup> Pottasch et al. (2003).<sup>d</sup> Hyung, Pottasch & Feibelman (2004).<sup>e</sup> Peimbert & Torres-Peimbert (1987).<sup>f</sup> Average abundances for 23 Galactic bulge PNe. Sample observed by Wang & Liu (2007) plus bulge PNe M 1-42 and M 2-36 analyzed by Liu et al. (2001).<sup>g</sup> Average abundances given by Wang & Liu (2007) for 58 Galactic disc PNe.<sup>h</sup> Solar values from Asplund et al. (2009).

of the NW knot is characterized by lines of intermediate-to-high excitation. Besides the H I Balmer lines, the strongest optical lines are [O II]  $\lambda$ 3727, [O III]  $\lambda\lambda$ 4959, 5007, [N II]  $\lambda\lambda$ 6548, 6583, and He II  $\lambda$ 4686. We also detect the strong, high excitation [Ne III]  $\lambda$ 3967 line in the NW knot. The intensities of the [O II]  $\lambda$ 3727, [N II]  $\lambda\lambda$ 6548, 6583 and [S II]  $\lambda\lambda$ 6716, 6731 emission lines rela-

tive to H $\beta$  are much stronger in the NW knot than in the inner and outer regions.

Figure 10 shows the observed line ratios in different regions of Hu 1-2 compared to those measured in the rims/shells and low-ionization structures of a sample of PNe using a set of diagnostic diagrams adopted from Raga et al. (2008). In these diagrams,

the data points associated to the rims and shells of PNe trace the locus of photoionized gas. The data points corresponding to low-ionization structures have been split into two different groups. The first one includes low-ionization structures that are projected inside the nebular shells (e.g., the FLIERs of NGC 6826), whereas the second group consists of those projected outside the nebular shells (e.g., the bow-shock features of IC 4634). This very simple classification is expected to assign mostly low-velocity photoionized structures to the first group, whereas the second group will be mostly populated by fast outflows, where irradiated shocks are expected to occur.

In the  $[S II]/H\alpha$  and  $[N II]/H\alpha$  versus  $[O III]/H\alpha$  diagrams, the data points of Hu 1-2 are located in the regions occupied by other PNe (Figure 10). In particular, the emission line ratios for the NW knot are compatible with those of the low-ionization structures in other PNe, with the  $[S II]/H\alpha$  and  $[N II]/H\alpha$  ratios consistently higher (by definition) than those derived for the photoionized rims and shells of PNe. Furthermore, the  $[O III]/H\alpha$  ratios of outflows tend to be higher than those of low-ionization structures projected inside the nebular shells. This can be evidence of an additional source of excitation, i.e., the shocks, particularly at larger distances from the central source, where the ionizing flux of photons is reduced and thus lower  $[O III]/H\alpha$  ratios would have been expected instead. It is also interesting to note that the NW knot of Hu 1-2 shows higher  $[O II]/[O III]$  and  $He II/H\alpha$  ratios than those typically seen in the low-ionization structures and outflows of other PNe. The  $He II/H\alpha$  ratios in the NW knot is also compatible with that observed in the inner region of Hu 1-2 (Figure 10, bottom right). These patterns observed in Hu 1-2 might be a consequence of the very high temperature of its central star (125 000 K; Hyung, Potasch & Feibelman 2004). The NW knot of Hu 1-2 probably harbors a significant amount of high-excitation material, and its relative amount of the high- to low-excitation material could be higher than that in the outflows and low-ionization structures of other PNe, making it a very peculiar structure.

The observed line ratios in the NW knot of Hu 1-2 are also compared in Figure 11 with the predictions for shocked regions in high-velocity knots of PNe developed by Raga et al. (2008). This comparison helps to diagnose the excitation mechanisms (photoionization, shocks, or both) in the NW knot. These models assume a cloudlet traveling away from a photoionizing source into a uniform medium ( $\sim 10^2 \text{ cm}^{-3}$ ). The simulations include transfer of the ionizing radiation and a non-equilibrium ionization network of many ionic species. In Figure 11, we present the predicted line ratios from an “ad hoc” model for Hu 1-2 where a high-density ( $\sim 10^3 \text{ cm}^{-3}$ ), high-velocity ( $v_c = 100, 150$  and  $250 \text{ km s}^{-1}$ ) cloudlet with the chemical abundances measured in Hu 1-2 is moving away from a 100 000-K central star. Cases with different distances from the central source ( $3 \times 10^{17}$ ,  $7 \times 10^{17}$  and  $3 \times 10^{18} \text{ cm}$ ) have been simulated. Those are axisymmetric simulations, and the initial temperature of the clump/cloudlet was set to be  $10^4 \text{ K}$ . In order to compare the observations and the numerical simulations, we integrated the computed emission line coefficients over the entire emitting volume to derive the emission line luminosities of the NW knot of Hu 1-2. Predicted line ratios for different integration times since the start of the shock are summarized in Table 6.

The predicted  $[S II]/H\alpha$ ,  $[N II]/H\alpha$ ,  $[O II]/[O III]$  and  $He II/H\alpha$  line ratios in Table 6 show a large scatter, but they are generally comparable to those derived from the observations of Hu 1-2. The plots in Figure 11 show that the best models to reproduce the observed line ratios in the NW knot of Hu 1-2 are those for a knot at distances of a few times  $10^{17} \text{ cm}$ . Models at the largest distance,

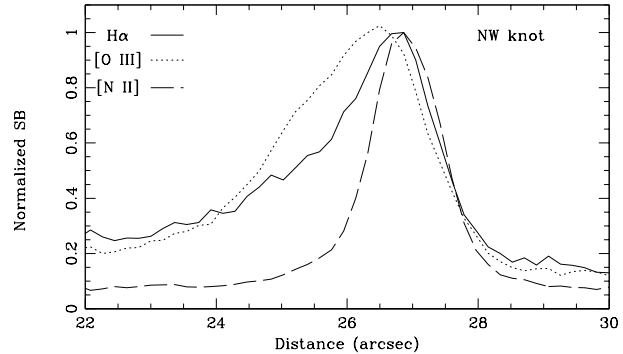


**Figure 8.** Brightness profiles of the  $[O III]$  (dotted line),  $H\alpha$  (solid line), and  $[N II]$  (dashed line) emission lines along the axis that connects the center of Hu 1-2 with the NW knot. The profiles have been normalized to their intensity peaks for a fair comparison. Distances are measured from the central star (in arcsec).

$3 \times 10^{18} \text{ cm}$ , generally predict too low  $[O III]/H\alpha$  ratios, which can be explained by the greater dilution of the ionizing flux from the central star. For models where the knot has smaller distances ( $\sim 10^{17} \text{ cm}$ ) from the central source (this is equivalent to changes in the ionizing flux at the clump), all predicted line ratios agree with those observed in the NW knot of Hu 1-2 within a factor of 2 to 3. Given the simplicity and limitations of our models (a spherical clump moving away from the central source through a constant medium, where the absorption of the photons by nebular gas between the star and the clump is not accounted for), the discrepancies between the observed line ratios and those predicted can be considered to be reasonable.

The plots in Figure 11 also help to constrain the knot velocity. Models at low velocity ( $100 \text{ km s}^{-1}$ ) tend to predict  $[S II]/H\alpha$ ,  $[N II]/H\alpha$ , and  $[O II]/[O III]$  line ratios lower than those observed in Hu 1-2. On the contrary, models at high velocity ( $250 \text{ km s}^{-1}$ ) predict too high values for these line ratios. Therefore, the knot velocity seems constrained in the range  $100\text{--}250 \text{ km s}^{-1}$ . We note that this knot velocity is smaller than the outflow velocity  $>340 \text{ km s}^{-1}$  derived from a spatio-kinematical model of the outflow (Miranda et al. 2012a).

Finally, we remark the persistent difficulty of our models to reproduce the observed  $[O III]/H\alpha$  line ratios. This issue can be alleviated by increasing the oxygen abundance assumed by our model. We tested this by increasing the oxygen abundance, and found that increasing the abundance within the uncertainty of our abundance determination produced some improvement (not shown in Figure 11); however it was insufficient to reproduce the observed  $[O III]/H\alpha$  line ratio.

#### 4.5 The jet-launching engine of Hu 1-2

The total mass, momentum and mechanical luminosity of the jets can be used to assess the jet-launching engine of a PN or proto-PN (e.g., Bujarrabal et al. 2001; Blackman & Lucchini 2014). Similar diagnosis is carried out for Hu 1-2 below. The ionized mass of the NW knot can be estimated from its  $H\beta$  flux. Using the total  $H\alpha$  flux of the NW knot derived from the NOT  $H\alpha$  flux-calibrated image presented in Figure 1 and the  $H\alpha$  to  $H\beta$  ratio derived 1-D spectrum in Table 2, we derived a total  $H\beta$  flux of  $\sim 3 \times 10^{-15} \text{ erg cm}^{-2} \text{ s}^{-1}$  for the NW knot. Adopting a distance of 3.5 kpc (Miranda et al. 2012a), and an angular radius of  $2''$ , an electron temperature of  $10^4 \text{ K}$ , and a filling factor of 0.4, we estimated an electron den-

**Table 6.** Shock model results compared with observations of the Hu 1-2 NW knot.

$v_c$ ( $\text{km s}^{-1}$ )	Distance ( $\times 10^{18}$ cm)	$t$ (years)	[O II]/H $\alpha$	[O III]/H $\alpha$	[N II]/H $\alpha$	[S II]/H $\alpha$	He II/H $\alpha$
100	0.3	50	0.280	1.000	0.340	0.028	0.380
		200	0.388	1.220	0.582	0.046	0.347
		350	0.118	1.580	0.145	0.018	0.421
100	0.7	50	0.468	0.915	0.839	0.120	0.176
		200	0.515	1.410	0.938	0.188	0.181
		350	0.482	1.870	0.802	0.129	0.193
100	3.0	50	0.519	0.094	1.090	0.393	0.011
		200	0.659	0.048	1.680	0.553	0.578
		350	0.826	0.060	2.070	0.554	0.022
150	0.3	50	0.588	0.882	0.916	0.062	0.313
		200	0.566	1.000	0.981	0.138	0.302
		350	0.384	1.400	0.622	0.085	0.343
150	0.7	50	0.588	0.882	0.951	0.196	0.164
		200	0.501	1.470	0.894	0.249	0.185
		350	0.439	1.920	0.705	0.179	0.200
150	3.0	50	0.684	0.130	1.120	0.468	0.233
		200	0.704	0.048	1.690	0.592	0.352
		350	0.835	0.060	2.040	0.597	0.429
250	0.3	40	0.838	0.666	1.486	0.132	0.250
		120	0.503	0.847	0.759	0.425	0.306
		200	0.401	1.276	0.606	0.278	0.346
250	0.7	40	0.815	0.775	1.025	0.283	0.146
		120	0.500	1.606	0.568	0.525	0.173
		200	0.477	2.047	0.600	0.352	0.188
250	3.0	40	0.943	0.217	1.132	0.535	0.017
		120	1.026	0.173	1.679	0.826	0.021
		200	0.946	1.056	1.925	0.683	0.020
Observations <sup>a</sup>			1.415	2.735	0.920	0.080	0.368

<sup>a</sup> Observations of the NW knot of Hu 1-2.

sity of  $\sim 200 \text{ cm}^{-3}$  and an ionized mass of  $\sim 2 \times 10^{-5} M_\odot$  for the bipolar knots of Hu 1-2.

The dynamical age of the bipolar knots of Hu 1-2 is well constrained to be 1375 yr under the assumption that the knots have been moving ballistically since their ejection (Miranda et al. 2012a). Under the same assumption, the ejection time-scale of these knots can be estimated from the ratio between their angular size,  $\sim 4''$ , and their distance to the central star,  $\sim 27''$ . This result in an ejection time-scale ( $\tau_{\text{jet}}$ )  $\sim 200$  yr. The averaged mass-loss rate during the ejection would then be  $\sim 1 \times 10^{-7} M_\odot \text{ yr}^{-1}$ .

The mechanical luminosity of the jets can be estimated using the equation

$$L_{\text{mec}} = \frac{\frac{1}{2} M_{\text{knot}} v_{\text{exp}}^2}{\tau_{\text{jet}}}, \quad (3)$$

where  $M_{\text{knot}}$  is the total ionized mass of the knots,  $v_{\text{exp}}$  is the expansion velocity ( $340 \text{ km s}^{-1}$ ; Miranda et al. 2012a), and  $\tau_{\text{jet}}$  is the jet ejection time-scale ( $\sim 200$  yr). Thus the jets mechanical luminosity of Hu 1-2 would be  $\sim 0.5 L_\odot$ . The total energy of the jets is  $\sim 1.2 \times 10^{43} \text{ erg}$ , which is lower than the kinetic energies of fast

**Table 7.** Physical properties of collimated outflows in PNe.

PN	$M_{\text{knot}}$ ( $M_\odot$ )	$v_{\text{exp}}$ ( $\text{km s}^{-1}$ )	$\tau_{\text{jet}}$ (yr)	$L_{\text{mec}}$ ( $L_\odot$ )
Hu 1-2	$\sim 2 \times 10^{-5}$	340	200	0.5
The Necklace <sup>a</sup>	$\sim 10^{-3}$	95(N), 115(S)	3700–8000	0.1–0.23
NGC 6778 <sup>a</sup>	$1.5 \times 10^{-3}$	270, 460	1700	5.3

<sup>a</sup> From Tocknell, De Marco & Wardle (2014).

outflows in proto-PNe (e.g., the sample studied by Bujarrabal et al. 2001) by at least one order of magnitude. The momentum estimated for the bipolar knots of Hu 1-2 is  $\sim 1.4 \times 10^{36} \text{ g cm s}^{-1}$ , also much lower than those ( $10^{37}$ – $10^{40} \text{ g cm s}^{-1}$ ) observed in proto-PNe, whose high linear momenta defy any easy interpretation (Bujarrabal et al. 2001).

The parameters associated to the jet launching in Hu 1-2 and those studied by Tocknell, De Marco & Wardle (2014) are presented in Table 7. A comparison among them indicates that the bipolar knots of Hu 1-2 are lighter, less massive than those of the



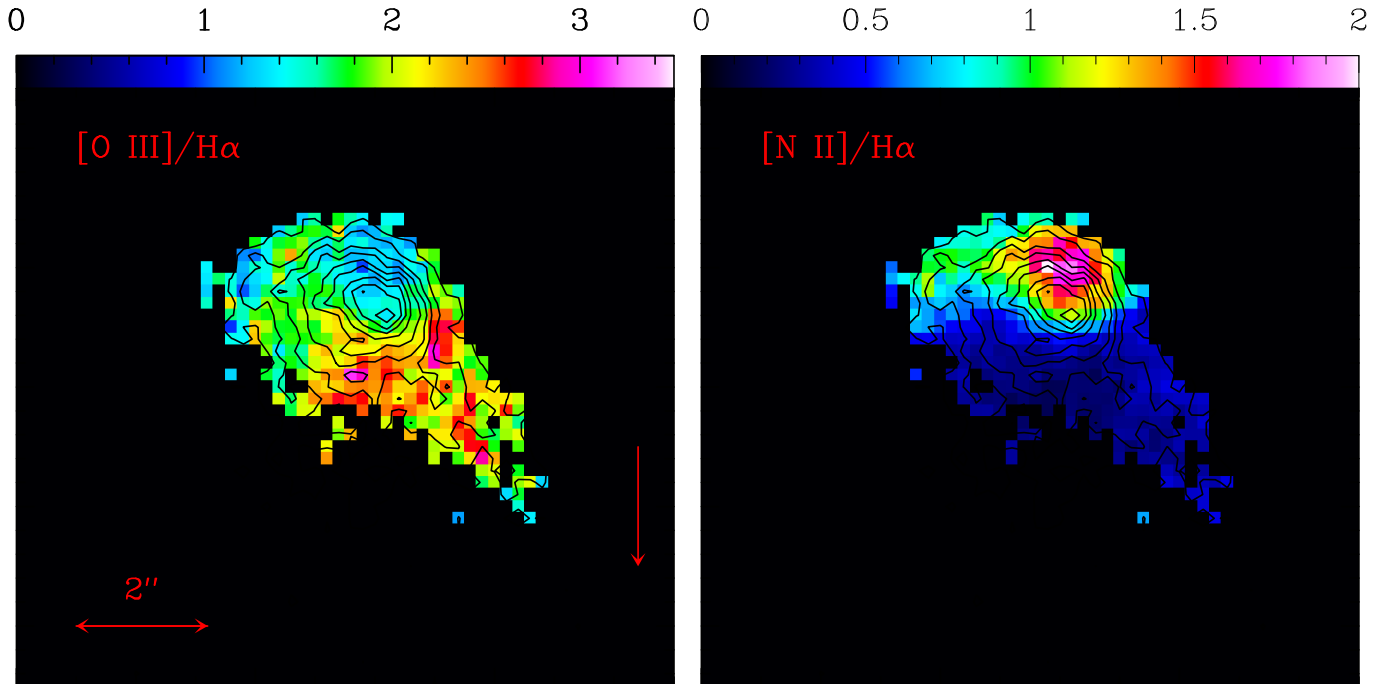


**Figure 9.**  $[\text{O III}]/\text{H}\alpha$  (left) and  $[\text{N II}]/\text{H}\alpha$  (right) ratio maps of the NW knot. The black contours over-plotted on the ratio maps trace the intensity in the  $\text{H}\alpha$  line. The red arrow in the left panel points to the direction of the central star of Hu 1-2.

Necklace Nebula and NGC 6778, whereas their ejection time-scale is much shorter. The two effects combined result in very similar mechanical luminosities for all sources in Table 7. We note the large uncertainty in the estimate of the ejection time-scale of the knots of Hu 1-2. Dynamical effects are certainly playing a crucial role in the evolution of the outflow, compressing the head of the flow (reducing the apparent ejection time-scale) or lagging material upstream (increasing the apparent ejection time-scale). Thus this ejection time-scale could be quite uncertain and so is the derived jets mechanical luminosity ( $L_{\text{mec}}$ ) of Hu 1-2.

It is interesting to note that the jets mechanical luminosity of NGC 6778 is extremely high (Table 7), if we adopt the parameters given in Tocknell, De Marco & Wardle (2014). This PN, which has a similar distance ( $\sim 2.6$  kpc; Tocknell, De Marco & Wardle 2014) as Hu 1-2, has a highly disrupted equatorial ring and a binary central star (Miszalski et al. 2011b; Guerrero & Miranda 2012). Both NGC 6778 and the Necklace Nebula in Table 7 have a post-common envelope (post-CE) close binary in the center (Miszalski et al. 2011b; Corradi et al. 2011). Like NGC 6778, Hu 1-2 displays an overall bipolar structure and a likely disrupted equatorial ring. This resemblance suggests that Hu 1-2 might have similar jet-launching mechanisms as the other two PNe.

## 5 CONCLUSIONS

We have presented a thorough imaging and spectroscopic study of the main nebular regions and bipolar outflows of Hu 1-2. The physical structure of the main nebula can be described as bipolar, although its velocity field cannot be described by a simple hour-glass law. The inclination of the bipolar lobes is  $\leq 10^\circ$  and its polar expansion velocity  $\simeq 150 \text{ km s}^{-1}$ , resulting in a lower-limit expansion age  $\lesssim 1100$  yr. Neither the morphology nor the kinematics of

the central, z-shaped innermost region of Hu 1-2 can be simply described as a waist or torus located between the two bipolar lobes. The knotty morphology of this region and its relatively high expansion velocity,  $\simeq 40 \text{ km s}^{-1}$ , are suggestive of a “broken” equatorial ring. The distorted velocity field of the bipolar lobes and the complex morphology of the equatorial regions make us conclude that Hu 1-2 has experienced notable violent dynamical processes during its formation. Similar interpretation has been given to the disrupted equatorial regions of a few bipolar PNe known to harbor binary systems (e.g., NGC 6778, NGC 7354; Contreras et al. 2010; Miszalski et al. 2011b; Guerrero & Miranda 2012). It is tempting to conclude that the fast bipolar knots present in all these sources are dynamical agents which caused the disrupted equatorial features.

It is interesting to remark here the apparent discrepancies implied by the chemical abundances of Hu 1-2. The high He/H and N/O abundance ratios suggest a Type I nature for Hu 1-2, which indicates that it descended from a relatively massive intermediate-mass progenitor star ( $\gtrsim 4 M_\odot$ ; e.g., Karakas et al. 2009). On the other hand, the low abundances of the heavy elements of Hu 1-2 suggest it formed long time ago, probably in an early-stage of the chemical evolution of the Galaxy, and thus it corresponds to a low-mass progenitor. Cases of Type I PNe with very low abundances of  $\alpha$  elements can be interpreted as a result of formation of a massive PN progenitor from unmixed (i.e., metal-poor) interstellar material (Milingo et al. 2010). Therefore, the chemical composition of Hu 1-2 probably does not represent that of its current environment. This might indeed be the case. At a galactocentric distance  $\sim 9$  kpc, as estimated from the distance to Hu 1-2 ( $\sim 3.5$  kpc; Miranda et al. 2012a), its Galactic longitude ( $86.5^\circ$ ) and the galactocentric distance of the Sun (8.3 kpc; Gillessen et al. 2009), the oxygen abundance of the interstellar medium is  $\sim 4 \times 10^{-4}$  (Henry et al. 2010, and Figure 1 therein), which is much higher than that of Hu 1-2 (see Table 5). Alternatively, Type I PNe have long been con-

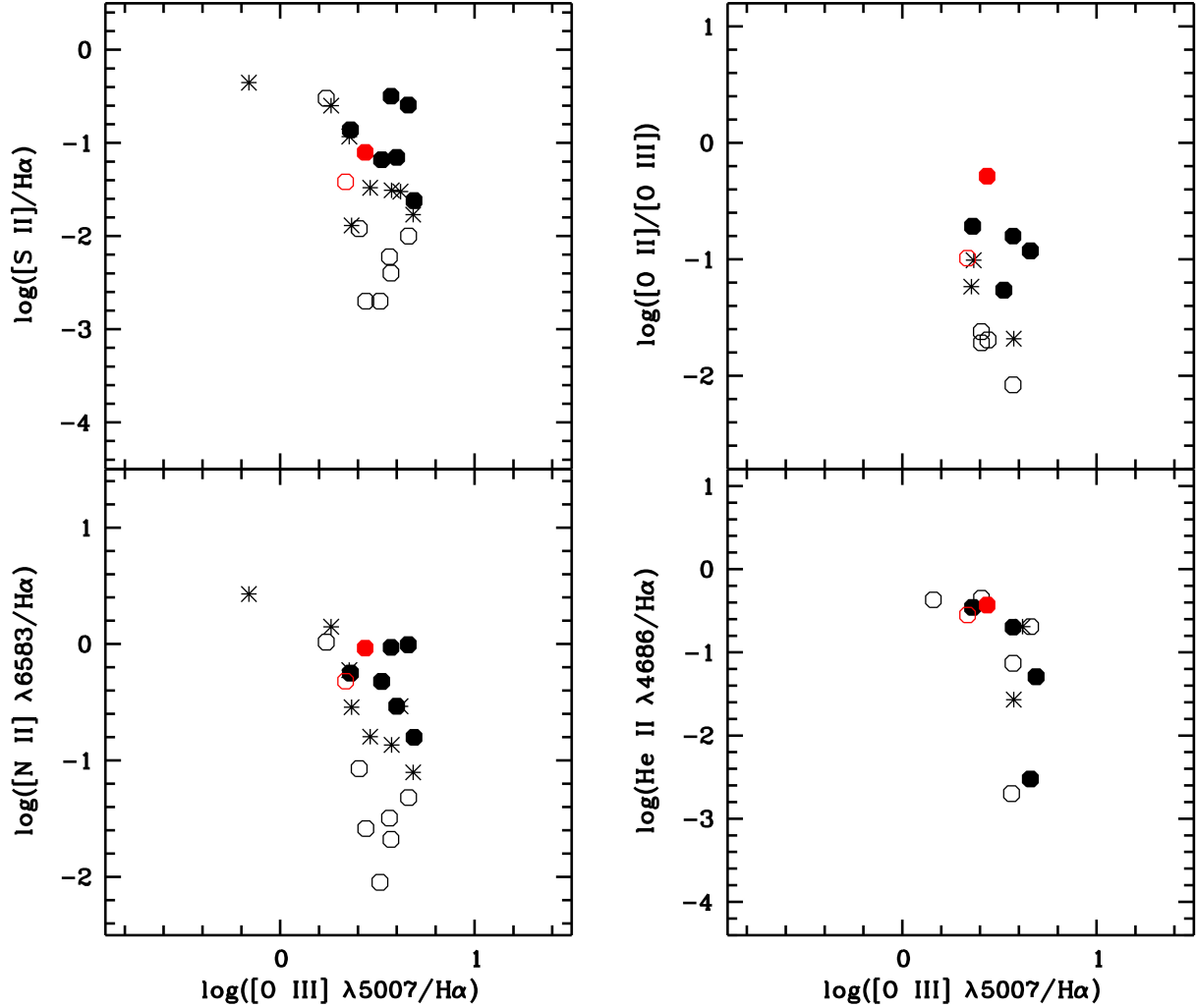


**Figure 10.** Diagnostic diagrams of several emission line ratios for rims/shells (open circles), low-ionization structures projected onto the nebular shells (stars), and outflows (filled circles) for a sample of PNe: ETHOS 1, He 1-1, IC 4634, K 1-2, KJpN 8, NGC 6543, NGC 6826, NGC 7009, NGC 7354, and NGC 7662 (Balick et al. 1994; Contreras et al. 2010; Exter, Pollacco & Bell 2003; Gonçalves et al. 2003, 2009; Guerrero et al. 2008; López-Martín et al. 2002; Miszalski et al. 2011a). The emission line ratios for Hu 1-2 are shown in red.

nected to bipolar morphology (e.g., Peimbert & Torres-Peimbert 1983) which is likely the result of binary interactions (e.g., Soker 1997) or common envelope binary interaction (e.g., Zijlstra 2007; De Marco 2009; Miszalski et al. 2009). The abundance pattern of Hu 1-2 might be due to the effects of binary interactions on the evolution of the progenitor and the composition of the subsequent PN, although so far it is not clear whether there is a binary central star in Hu 1-2. Detailed discussion of this point is beyond the scope of this paper. We also discussed the possibility of Hu 1-2 being a halo PN, given that it is quite out of the Galactic plane ( $b = -8^\circ 8$ ). Although the oxygen abundances of Hu 1-2 and its distance to the Galactic plane marginally support a halo nature, its low peculiar radial velocity obviously argues against a halo nature for Hu 1-2.

The collimated bipolar outflows of Hu 1-2 are particularly interesting. They show a notable bow-shock-like morphology. The emission within these structures is found to be highly stratified, with [N II] peaking at the leading edge of the bow-shock and [O III] mostly occupying the star-facing region. This profile is similar to that found in the bow-shock structures of PNe such as IC 4634 and NGC 7009. Previous spatio-kinematical studies have suggested an

expansion velocity  $>340 \text{ km s}^{-1}$  for the outer knots of Hu 1-2. This high expansion velocity of the bipolar knots, together with the bow-shock-like morphology associated with them, indicate that the high-velocity, collimated bipolar outflows are moving through the interstellar medium like “bullets”.

The line ratios of the NW knot of Hu 1-2 and those from the collimated outflows of other PNe are generally consistent with those of other low-ionization structures, but they exhibit higher [O III]/H $\alpha$  ratios. This line ratio is particularly high in Hu 1-2, indicating that both low- and high-excitation gas are present at the location of this feature with significant amounts. The observed line ratios of the NW knot of Hu 1-2 have been modeled using “ad hoc” simulations of a fast moving cloudlet in a medium with homogeneous density. The model predictions are generally consistent with the observed line ratios, thus confirming that the excitation of the bipolar knots of Hu 1-2 can be explained by a mix of the UV radiation and shocks. The models favor distance, nebular abundances, and stellar parameters consistent with those derived for Hu 1-2. As reported for the collimated outflows of other PNe and proto-PNe (e.g., Hen 3-1475; Riera et al. 2006), the best knot velocity

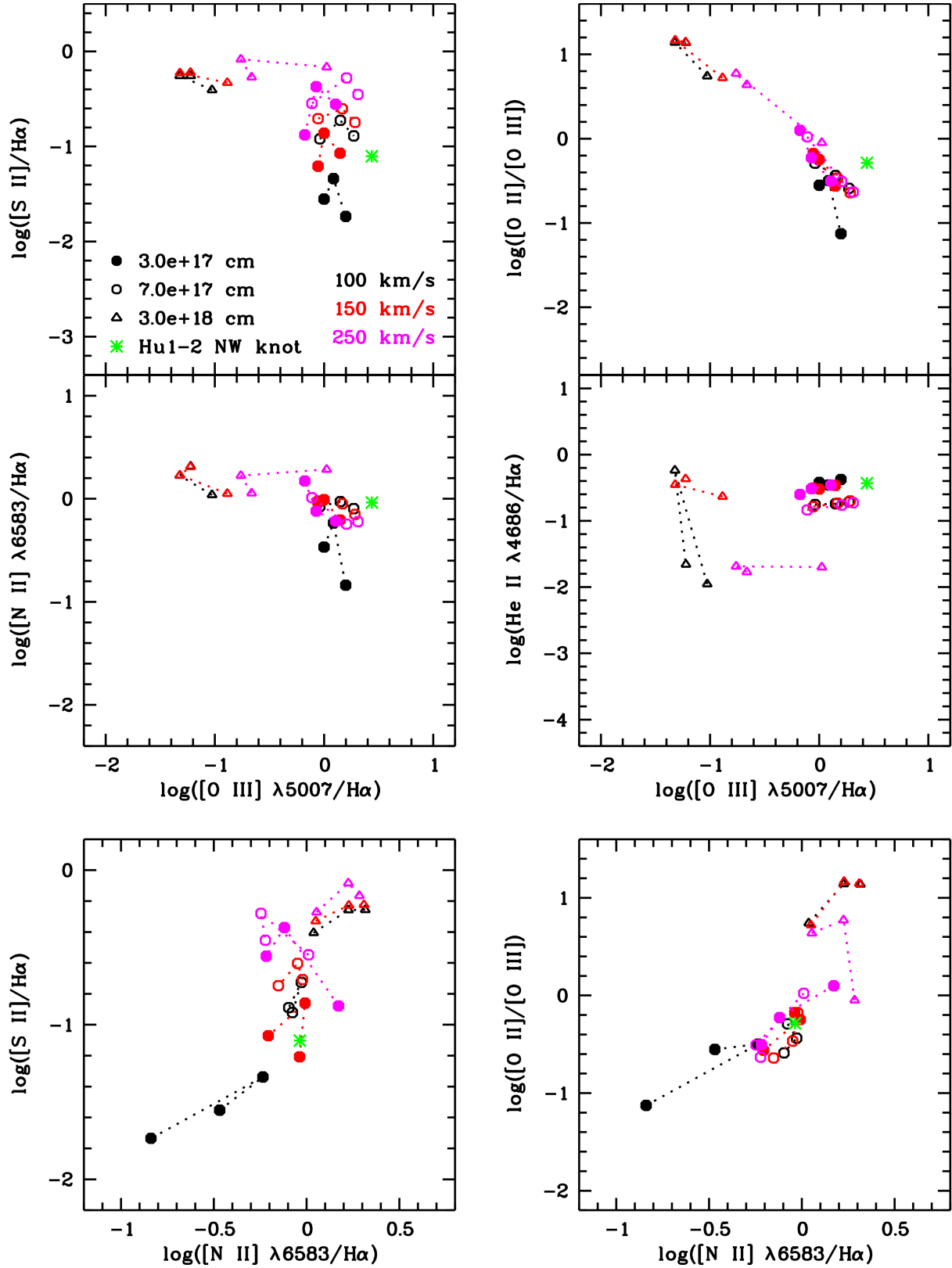


**Figure 11.** Similar to Figure 10, but comparing the emission line ratios predicted for a shocked cloudlet moving away from a photoionizing source with those seen in the NW knot of Hu 1-2 (the green star) for different distances from the central star and at different expansion velocities (see description of the symbols in the upper-left panel). Symbols of the same models are connected with dotted lines to show the time-evolution sequences.

(100–250 km s<sup>-1</sup>) inferred from the models is below that derived by spatio-kinematical studies (>340 km s<sup>-1</sup>).

Finally, we estimated the ionized mass of the NW knot of Hu 1-2, and calculated the jets mechanical luminosity using the knots' mass and the ejection time-scale based on the dynamical age of the bipolar outflow. The jets mechanical luminosity and the mass-loss rate of Hu 1-2 generally agree, within the uncertainties, with those of the Necklace and NGC 6778, both of which have a post-common envelope close binary central star. The resemblance of Hu 1-2 with NGC 6778 in nebular structure and morphology hints at a possibility that the former might have similar jet-launching engine as the latter.

## ACKNOWLEDGEMENTS

XF and MAG acknowledge support from grant AYA 2011-29754-C03-02. LFM is partially supported by grant AYA2011-30228-C3-01 (co-funded by FEDER funds) of the Spanish MICINN. AR is supported by grant MINECO AYA2011-30228-C03 (Spain). PFV and ACR are supported by CONACyT grant 167611 and DGAPA-PAPIIT (UNAM) grant IG100214. This paper is based on observations made with the 1.5m telescope operated by the Instituto de Astrofísica de Andalucía at the Observatorio de Sierra Nevada, Granada, Spain, and with the Nordic Optical Telescope (NOT) and the Italian Telescopio Nazionale Galileo (TNG) operated at the Observatorio del Roque de los Muchachos, La Palma, Spain, by the Nordic Optical Telescope Scientific Association and the Fundación Galileo Galilei of the INAF (Istituto Nazionale di Astrofisica), respectively. We thank Orsola De Marco, the referee of this article, for her insightful comments which have greatly improved the quality of this article.

## REFERENCES

- Aller L. H., Czyzak S. J., 1979, *Ap&SS*, 62, 397
- Asplund M., Grevesse N., Sauval A. J., Scott P., 2009, *ARA&A*, 47, 481
- Balick B., Alexander J., Hajian A. R., Terzian Y., Perinotto M., Patriarchi P., 1998, *AJ*, 116, 360
- Balick B., Frank A., 2002, *ARA&A*, 40, 439
- Balick B., Perinotto M., Maccioni A., Terzian Y., Hajian A., 1994, *ApJ*, 424, 800
- Benjamin R. A., Skillman E. D., Smits D. P., 1999, *ApJ*, 514, 307
- Blackman E. G., Lucchini S., 2014, *MNRAS*, 440, L16
- Bujarrabal V., Castro-Carrizo A., Alcolea J., Sánchez Contreras C., 2001, *A&A*, 377, 868
- Cardelli J. A., Clayton G. C., Mathis J. S., 1989, *ApJ*, 345, 245
- Contreras M. E., Vázquez R., Miranda L. F., et al., 2010, *AJ*, 139, 1426
- Corradi R. L. M., Sabin L., Miszalski B., et al., 2011, *MNRAS*, 410, 1349
- Dennis T. J., Cunningham A. J., Frank A., Balick B., Blackman E. G., Mitran S., 2008, *ApJ*, 679, 1327
- Durand S., Acker A., Zijlstra A., 1998, *A&AS*, 132, 13
- Exter K. M., Pollacco D. L., Bell S. A., 2003, *MNRAS*, 341, 1349
- De Marco O., 2009, *PASP*, 121, 316
- Gillessen S., Eisenhauer F., Trippe S., Alexander T., Genzel R., Martins F., Ott T., 2009, *ApJ*, 692, 1075
- Gonçalves D. R., Corradi R. L. M., Mampaso A., Perinotto M., 2003, *ApJ*, 597, 975
- Gonçalves D. R., Mampaso A., Corradi R. L. M., Quireza C., 2009, *MNRAS*, 398, 2166
- Guerrero M. A., Miranda L. F., 2012, *A&A*, 539, A47
- Guerrero M. A., Miranda L. F., Chu Y.-H., *Rev. Mex. Astron. Astrofís.*, 12, 156
- Guerrero M. A., Miranda L. F., Ramos-Larios G., Vázquez R., 2013, *A&A*, 551, A53
- Guerrero M. A., Miranda L. F., Riera A., Velázquez P. F., Olguín L., Vázquez R., Chu Y.-H., Raga A., Benítez G., 2008, *ApJ*, 683, 272
- Hartigan P., Raymond J., Hartmann L., 1987, *ApJ*, 316, 323
- Henry R. B. C., Kwitter K. B., Jaskot A. E., Balick B., Morrison M. A., Milingo J. B., 2010, *ApJ*, 724, 748
- Howard J. W., Henry R. B. C., McCartney S., 1997, *MNRAS*, 284, 465
- Huarte-Espinosa M., Frank A., Balick B., Blackman E. G., De Marco O., Kastner J. H., Sahai R., 2012, *MNRAS*, 424, 2055
- Humason M. L., 1921, *PASP*, 33, 175
- Hyung S., Pottasch S. R., Feibelman W. A., 2004, *A&A*, 425, 143
- Karakas A. I., Lattanzio J. C., 2003, *PASA*, 20, 393
- Karakas A. I., van Raai M. A., van Lugaro M., Sterling N. C., Dinerstein H. L., 2009, *ApJ*, 690, 1130
- Kingsburg R. L., Barlow M. J., 1994, *MNRAS*, 271, 257
- Kwitter K. B., Henry R. B. C., Jaskot A. E., Balick B., 2010, *AAS*, 42, 472
- Liu X.-W., Luo S.-G., Barlow M. J., Danziger I. J., Storey P. J., 2001, *MNRAS*, 327, 141
- López-Martín L., López J. A., Esteban C., Vázquez R., Raga A., Torrelles J. M., Miranda L. F., Meaburn J., Olguín L., 2002, *A&A*, 388, 652
- Manchado A., Guerrero M. A., Stanghellini L., Serra-Ricart M., 1996, *IAC Morphological Catalog of Northern Planetary Nebulae*. IAC, La Laguna
- Milingo J. B., Kwitter K. B., Henry R. B. C., Souza S. P., 2010, *ApJ*, 711, 619
- Miranda L. F., Blanco M., Guerrero M. A., Riera A., 2012a, *MNRAS*, 421, 1661
- Miranda L. F., Blanco M., Guerrero M. A., Riera A., 2012b, *IAUS*, 283, 440
- Miranda L. F., Torrelles J. M., Guerrero M. A., Vázquez R., Gómez Y., 2001, *MNRAS*, 321, 487
- Miszalski B., Acker A., Parker Q. A., Moffat A. F. J., 2009, *A&A*, 505, 249
- Miszalski B., Corradi R. L. M., Boffin H. M. J., et al., 2011a, *MNRAS*, 413, 1264
- Miszalski B., Jones D., Rodríguez-Gil P., et al., 2011b, *A&A*, 531, A158
- Nordhaus J., Blackman E. G., 2006, *MNRAS*, 370, 2004
- Olofsson H., Maercker M., Eriksson K., Gustafsson B., Schöier F., 2010, *A&A*, 511, A27
- Peimbert M., 1990, *MNRAS, Rep. Prog. Phys.*, 53, 1559
- Peimbert M., Luridiana V., Torres-Peimbert S., 1995, *Rev. Mex. Astron. Astrofís.*, 31, 147
- Peimbert M., Torres-Peimbert S., 1983, *IAUS*, 103, 233
- Peimbert M., Torres-Peimbert S., 1987, *Rev. Mex. Astron. Astrofís.*, 14, 540
- Peña M., Rechy-García J. S., García-Rojas J., 2013, *Rev. Mex. Astron. Astrofís.*, 49, 87
- Pottasch S. R., Hyung S., Aller L. H., Beintema D. A., Bernard-Salas J., Feibelman W. A., Klöckner H. R., 2003, *A&A*, 401, 205
- Raga A. C., Riera A., Mellema G., Esquivel A., Velázquez P. F., 2008, *A&A*, 489, 1141

- Reay N. K., Atherton P. D., 1985, MNRAS, 215, 233  
Reyes-Ruiz M., López J. A. 1999, ApJ, 524, 952  
Riera A., Binette L., Raga A. C., 2006, MNRAS, 203, 213  
Riera A., Raga A. C., Asymmetrical Planetary Nebulae IV, 14  
Sabbadin F., Bianchini A., Hamzaoglu E., 1983, A&AS, 51, 119  
Sabbadin F., Cappellaro E., Turatto M., 1987, A&A, 182, 305  
Sahai R., Trauger J. T., 1998, AJ, 116, 1357  
Savage B. D., Mathis J. S., 1979, ARA&A, 17, 73  
Schneider S. E., Terzian Y., Purgathofer A., Perinotto M., 1983, ApJS, 52, 399  
Soker N., 1997, ApJS, 112, 487  
Soker N., 1998, ApJ, 496, 833  
Soker N., 2006, ApJL, 645, L57  
Soker N., Livio M., 1994, ApJ, 421, 219  
Solf J., Ulrich H., 1985, A&A, 148, 274  
Storey P. J., Hummer D. G., 1995, MNRAS, 272, 41  
Tocknell J., De Marco O., Wardle M., 2014, MNRAS, 439, 2014  
Wang W., Liu X.-W., 2007, MNRAS, 381, 669  
Wang W., Liu X.-W., 2008, MNRAS, 389, L33  
Whitford A. E., 1958, AJ, 63, 201  
Zijlstra A. A., 2007, Balt. Astron., 16, 79